On the impact of turbulent inflow and crack-induced blunt trailing edge on the flow field and far-field noise of an airfoil

RESEARCH ARTICLE | OCTOBER 17 2025

# On the impact of turbulent inflow and crack-induced blunt trailing edge on the flow field and far-field noise of an airfoil

Yanan Zhang ; Simon Watson ; Daniele Ragni ; Francesco Avallone



*Physics of Fluids* 37, 105145 (2025)
https://doi.org/10.1063/5.0299883

Physics of Fluids ARTICLE pubs.aip.org/aip/pof

# On the impact of turbulent inflow and crack-induced blunt trailing edge on the flow field and far-field noise of an airfoil

Cite as: Phys. Fluids **37**, 105145 (2025); doi: 10.1063/5.0299883
Submitted: 29 August 2025 · Accepted: 29 September 2025 ·
Published Online: 17 October 2025



Yanan Zhang,[1,a)] Simon Watson,[1] Daniele Ragni,[1] and Francesco Avallone[2]

## AFFILIATIONS

[1]Wind Energy Section, Faculty of Aerospace Engineering, Delft University of Technology, Delft 2629HS, The Netherlands
[2]Department of Mechanical and Aerospace Engineering, Politecnico di Torino, Turin 10129, Italy

[a)]Author to whom correspondence should be addressed: Yanan.Zhang@tudelft.nl

## ABSTRACT

An experimental investigation is carried out to characterize the physical mechanisms by which a trailing-edge crack, idealized as a rectangular cavity to represent delamination damage, affects boundary layer development, coherent vortex shedding, and far-field noise of a National Advisory Committee for Aeronautics 0018 airfoil. Both clean and turbulent inflow conditions are considered to isolate the role of inflow disturbance in modifying these mechanisms. The primary objective is to gain insight into how a geometrical discontinuity at the trailing edge alters the coupled aerodynamic and aeroacoustic behavior. Far-field acoustic measurements and near-wake velocity field data are obtained in the anechoic wind tunnel at Delft University of Technology. Acoustic data from a phased microphone array (from prior work) are combined with new velocity field measurements using particle image velocimetry. The results reveal that increasing crack size leads to enhanced near-wall velocity gradients and stronger coherent vortex shedding, resulting in higher tonal noise levels, particularly at higher frequencies. Normalized tonal frequencies agree with the empirical prediction model of Brooks, Pope, and Marcolini for blunt trailing-edge noise, affirming the relevance of this model even in the presence of geometric imperfections. Under turbulent inflow, the coherent structure scale diminishes slightly, and the tonal frequency increases in the trailing-edge noise spectrum, indicating that inflow turbulence modifies the vortex shedding dynamics and should be accounted for in predictive models. This study is a first step toward understanding and modeling trailing-edge noise in the presence of structural damage, under varying flow conditions.





## I. INTRODUCTION

In recent years, wind energy has established itself an important contributor in the transition to renewable electricity generation, attracting increasing interest from both industry and academia.[1,2] However, wind turbine blades are frequently subjected to damage, which deteriorates their aerodynamic performance[3] and, in severe cases, leads to full system failure.[4] Therefore, effective blade health condition monitoring and damage detection have become increasingly important to maintain reliable power output and safe operation of wind turbines. Continuous monitoring can be helpful in assessing the severity of damage and predicting its development. Established techniques for blade damage detection generally rely on measurements of vibration,[5,6] strain,[7] or acoustic emission (AE).[8] These techniques adopt one or multiple sensors mounted on or in the blade requiring cumbersome retrofitting for wind turbines that are already operational. For this reason, non-contact approaches are being developed, such as infrared thermography[9] and laser scanning techniques.[10]

Wind turbine noise has been a crucial issue to be mitigated to meet installation regulations and social acceptance,[11] in particular for onshore wind farms. Since aerodynamic noise from a wind turbine is one of the most important noise sources, many studies have been conducted to reduce it by adjusting the geometry of the airfoils,[12–14] adding serrations,[15,16] or adopting porous materials.[17–20] These techniques are standard approaches for noise reduction, on which some benchmark studies have focused.[21,22] These studies have inspired a new application of aeroacoustics for wind turbine blade damage detection using microphones in the far-field.[23–26] The working principle is based upon the modifications to the flow field that surface damage causes, which in turn affect aerodynamically generated noise.[25,27,28]

The aeroacoustics-based approach potentially enables real-time, passive monitoring of rotating wind turbine blades without requiring turbine shutdowns or complex instrumentation, offering a simpler and more cost-effective alternative complementing traditional methods like laser-based[29] or thermal imaging[30,31] for more comprehensive damage assessment.

Previous studies by the authors[25,26] proved that, under some circumstances, measurements of aerodynamic noise can provide useful information for blade damage detection. For example, in the presence of leading-edge erosion, it has been found that the leading-edge impingement noise has lower high-frequency spectral content with respect to that measured for a baseline reference airfoil. This was attributed to a larger stagnation region[14,32] formed in front of the eroded leading edge and to a consequent reduction in the magnitude of the surface pressure fluctuations at the leading edge.[27] It was further observed that the difference in the spectral peak sound pressure level between the baseline airfoil and one with an eroded leading edge, $\Delta L_p = L_{p,\text{Baseline}} - L_{p,\text{Erosion}}$, occurs at a chord-length-based Strouhal number $St_C \sim 10$. Moreover, the amplitude of $\Delta L_p$ increases as the size of the damage increases.

By contrast, when a crack appears at the trailing edge, this results in an effectively thicker trailing edge that can cause blunt trailing-edge noise. It is known from the literature that, when the trailing-edge thickness, $h$, is approximately larger than 0.3 times the boundary layer displacement thickness, $\delta^*$, periodic vortex shedding appears causing tonal noise.[33–35] The frequency and amplitude of the tonal peaks depend on the ratio of trailing edge to boundary layer displacement thickness, $h/\delta^*$, and it usually appears at trailing-edge-thickness-based Strouhal number $St_h \sim 0.1$.[36] In the authors' previous work,[25] it was investigated how the trailing-edge crack and the operational conditions affect the trailing-edge noise spectra, in particular the crack-induced tones.

While the authors' previous work[25] provided a detailed acoustic characterization of the noise generated by a cracked trailing edge, it did not investigate the underlying aerodynamic mechanisms responsible for the observed changes in the noise spectra, due to the absence of flow field measurements. As a result, a fundamental understanding of how trailing-edge damage and varying inflow conditions influence key flow features, such as local velocity gradients, turbulent boundary layer development, and coherent vortex shedding, is still lacking. These aerodynamic features are known to directly affect tonal noise generation.[37,38] Gaining such insight is essential to assess whether semi-empirical models for blunt trailing-edge noise[36] remain valid in the presence of structural damage at the trailing edge, and whether their predictive accuracy holds under both uniform and turbulent inflow conditions.

This investigation is motivated by the acoustic observation in the authors' prior work that, when inflow turbulence is introduced, the crack-induced tonal peak shifts to a higher trailing-edge-thickness-based Strouhal number, $St_{h,\text{peak}}$.[25] This behavior contrasts with established findings in the literature, which report that turbulent free-stream conditions lead to earlier boundary layer transition, faster downstream development, and increased boundary layer thickness.[39–42] According to semi-empirical models developed for clean inflow conditions,[36] an increase in boundary layer thickness would typically reduce the Strouhal number associated with blunt trailing-edge noise. Therefore, the upward frequency shift observed under turbulent inflow in the authors' previous acoustic study appears inconsistent with existing predictive models, revealing a gap in understanding how inflow turbulence interacts with trailing-edge damage to modify flow-induced tonal noise.

This inconsistency points to the need for a better understanding of how a cracked trailing edge alters flow mechanisms, particularly under turbulent conditions. Several studies have investigated the effect of free-stream turbulence on trailing-edge noise through measurements of boundary layer integral parameters and surface pressure fluctuations and of far-field acoustic spectra.[43,44] Findings suggested that the free-stream turbulence affects the turbulent structures within the boundary layers and their coherence even at high frequencies, thus changing the trailing-edge noise spectra.[45,46] Prior fundamental studies on vortex shedding from cylinders[47–49] have shown that free-stream turbulence disrupts the formation and coherence of large-scale wake vortices, resulting in smaller, fragmented structures and a shift of the wake energy spectrum toward higher frequencies with broader spectral content. These effects have been attributed to the destabilization of shear layers and accelerated vortex breakdown. While these insights align qualitatively with the acoustic trends observed in the authors' earlier work, they do not directly address whether similar mechanisms govern vortex formation and evolution behind a cracked (blunt) trailing edge.

The present study addresses this gap by examining how a simplified rectangular trailing-edge crack, intended to mimic delamination damage,[50] modifies the near-wall velocity gradients and coherent vortex structures in the near wake, under both clean and turbulent inflow conditions. By linking these aerodynamic changes to corresponding acoustic measurements, the study aims to build foundational knowledge necessary to assess the applicability and limitations of existing semi-empirical models for crack size estimation in turbulent inflow environments.[36]

To this end, the present study extends previous acoustic investigations by incorporating detailed flow field measurements to uncover the aerodynamic mechanisms underlying the observed tonal noise behavior. While earlier work focused on far-field noise characterization using a phased microphone array in combination with beamforming techniques,[51,52] the current study complements these findings with velocity field measurements near the trailing edge and in the near wake of a National Advisory Committee for Aeronautics (NACA) 0018 airfoil featuring various crack sizes. These measurements are performed under both clean and turbulent inflow conditions using particle image velocimetry (PIV).[53,54] To further investigate vortex shedding dynamics, proper orthogonal decomposition (POD) is applied to the PIV data to extract the dominant coherent structures.[53,54] Finally, the experimental results are evaluated against predictions from the Brooks–Pope–Marcolini (BPM) semi-empirical model for trailing-edge noise,[36] to assess its validity in the presence of structural damage and under varying inflow conditions.

The rest of the paper is organized as follows: Sec. II presents the experimental setup and the methodologies used for post-processing both the acoustic and aerodynamic measurements. In Sec. III, the experimental results and the relationship between the acoustic and aerodynamic data are reported and the interpretation of the change of the crack-induced tone is also discussed. Section IV summarizes the findings of this study and provides recommendations for the next steps.

## II. EXPERIMENTAL SETUP AND METHODOLOGY

### A. Facilities and test models

The experiments were carried out in the anechoic vertical open-jet wind tunnel (A-tunnel) of the Delft University of Technology,[55] shown in Fig. 1, where the turbulence intensity of the clean inflow is less than 0.1%. Absorbent foam wedges, with a height of 0.49 m, are placed on the walls of the test room; the acoustic cutoff frequency is 173.5 Hz; the A-weighted overall background noise levels vary from 35 to 64 dBA as the free-stream velocity increases from 10 m/s to 40 m/s. Additional details on the wind tunnel characteristics can be found in Ref. 55. To mimic the turbulent inflow conditions, a grid was designed and mounted on the nozzle of the wind tunnel providing a turbulent inflow with a turbulence intensity level of $I = 4.0\%$ and an integral length scale of $\Lambda_f = 7.9$ mm. A detailed characterization of the inflow turbulence can be found in Ref. 25.

A NACA 0018 airfoil with a chord length of $C = 200$ mm and a span of $L = 400$ mm was tested, where the leading edge was placed at a height of 0.3 m with respect to the wind tunnel nozzle. The trailing edge of the airfoil is changeable, which allows the testing of different trailing-edge configurations with different crack sizes. Each crack was designed as a rectangular gap with a given width, $W$, and depth, $D = 1.5W$. The dimensions of the trailing-edge cracks investigated are reported in Table I. Consequently, the thickness of the trailing edge, $h$, is equal to $h_{\text{Baseline}} + W$ (where $h_{\text{Baseline}}$ is the trailing-edge thickness of the baseline). Figure 2 shows the baseline airfoil and an example of the trailing edge with a crack width of 0.2 mm. Due to the nature of the open test section of the wind tunnel, the effective angle of attack, $\alpha^*$, is lower than the geometrical one, $\alpha$; more specifically, $\alpha^*/\alpha = 0.48$.[25]

The tests were carried out at mean inflow velocities equal to $U_\infty = 15$, 20, 25, 30, and 35 m/s, which correspond to the chord-length-based Reynolds numbers of $Re_C = 2.0 \times 10^5$, $2.7 \times 10^5$, $3.4 \times 10^5$, $4.1 \times 10^5$, and $4.7 \times 10^5$, respectively. Due to the low Reynolds number conditions, the flow was forced to transition using carborundum tape at 20% of the chord location on both the suction and pressure sides. The average carborundum roughness element size was 0.84 mm.

**TABLE I.** The dimensions of the cracked trailing edges.

| Trailing edge No. | 0 (Baseline) | 1 | 2 | 3 | 4 |
|---|---|---|---|---|---|
| $W$ (mm) | 0 | 0.20 | 0.50 | 1.00 | 2.00 |
| $h$ (mm) | 0.76 | 0.96 | 1.26 | 1.76 | 2.76 |
| $W/C$ (%) | 0 | 0.10 | 0.25 | 0.50 | 1.00 |
| $h/C$ (%) | 0.38 | 0.48 | 0.63 | 0.88 | 1.38 |

### B. Acoustic measurements

Noise measurements were conducted using a 2-D planar microphone array with 64 *G.R.A.S. 40PH* free-field microphones, as shown in Fig. 1. The microphone array was placed at 1 m from the airfoil trailing edge. The sampling frequency of each microphone is 51.2 kHz, and the signal was recorded for 20 s for each case. The signal was separated into chunks with 5120 samples ($\Delta t = 0.1$ s) for each Fourier transform (with a Hanning weighting function and 50% data overlap), and the spectrum was averaged over all chunks. The final spectral resolution is equal to 10 Hz. Conventional frequency-domain beamforming[51,52] was then carried out on the plane where the trailing edge is located. In this study, the trailing-edge noise is of interest; therefore, the source power integration[56] was performed on a 0.2 m × 0.2 m square area centered at the mid-span of the trailing edge. The detailed setup for the acoustic measurements was reported in Ref. 25.

The sound pressure level (SPL, $L_p = 10 \log\left(\frac{p'^2}{p_{\text{ref}}^2}\right)$, where $p'$ and $p_{\text{ref}}$ are the root mean square of sound pressure fluctuations and reference pressure of 20 μPa for air, respectively) is used as the metric for the far-field noise spectra. In this study, the measured $L_p$ of trailing-edge noise was obtained from the beamforming and the source power integration. The measured sound pressure levels of the airfoil trailing-edge noise are more than 10 dB above the background noise within the frequency bands 500–2000 and 500–1500 Hz for the clean and turbulent inflow conditions, respectively.[25]

The relative sound pressure level, $\Delta L_p$, is used to compare the sound pressure level resulting from the cracked cases with that from the baseline and is defined as

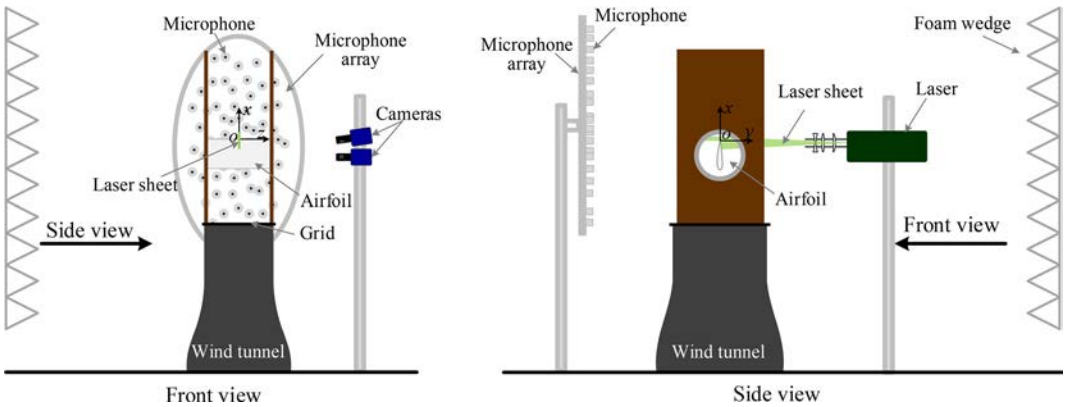


**FIG. 1.** Experimental setup.

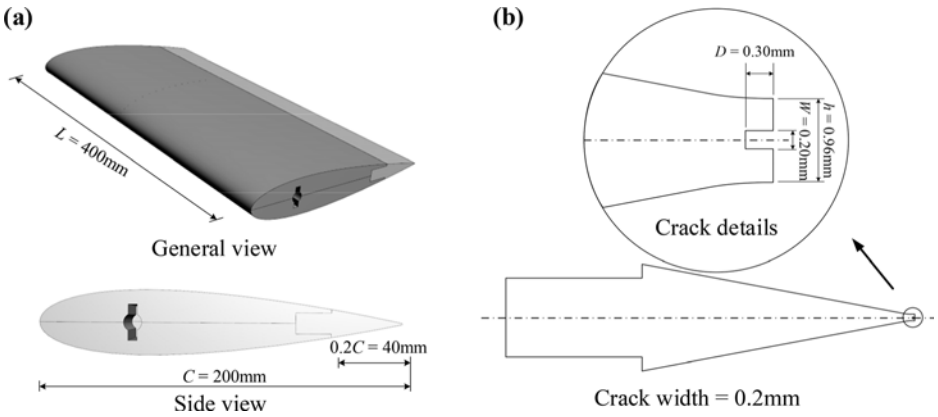


FIG. 2. The test airfoil: (a) baseline (a trailing edge insert without a crack) and (b) an example of a trailing edge insert with a 0.2 mm crack.

$$\Delta L_p = L_p - L_{p,\text{Baseline}}. \tag{1}$$

The frequency, $f$, is nondimensionalized by trailing-edge-thickness-based Strouhal number, i.e., $St_h = \frac{fh}{U_\infty}$, where $U_\infty$ is the inflow mean velocity. In order to estimate the frequency of the tonal peak of $\Delta L_p$, an analytical curve of the form

$$\Delta L'_p = Ae^{\left(St_h - St'_{h,\text{peak}}\right)^2} + B_{\text{offset}} \tag{2}$$

is used, where $\Delta L'_p$ denotes the best fit to the values of $\Delta L_p$; $St'_{h,\text{peak}}$ the estimated location of the tonal peak; and $A$ and $B_{\text{offset}}$ are the fitting coefficients determining the amplitude and offset of the curve. Figure 3 shows examples of the fit for the $W = 2.0$ mm case with both clean and turbulent ($I = 4.0\%$) inflow conditions.

### C. Velocity field measurements

The measurements of the velocity fields near the trailing edge and in the near wake were performed using PIV. The setup for PIV measurements is shown in Fig. 1. The seeding particles were produced by the SAFEX Twin-Fog Double Power fog generator, which provided a mean droplet diameter of 1 μm (it is integrated into the wind tunnel and not shown in Fig. 1). An EverGreen 200 laser was used as the light source. It provided a dual-pulsed beam of 532 nm wavelength with a maximum pulse frequency of 15 Hz and a maximum pulse energy of 200 mJ. The pulse frequency was set to 10 Hz, and the energy was set to 55% of the maximum. The laser beam was turned into a 2-mm-thick sheet by three lenses.

Two LaVision sCMOS cameras were used to record particle images. One was used to measure the velocity field and the boundary layer near the trailing edge, while the other was used to measure the near-wake velocity field. Each camera has a sensor with a size of 2560 × 2160 pixels and the pixel pitch of 6.5 μm. A Nikon NIKKOR prime lens with a focal length $f' = 200$ mm was mounted on each camera. The focus plane was adjusted to the middle span of the airfoil, which was illuminated by the laser sheet. The aperture was set to $f'/8.0$, which provided the proper depth of field for this experiment. The field of view for each camera is approximately 32 × 27 mm. The two fields of view are shown in Fig. 4. A right-hand $xoy$ coordinate system was established at the middle span of the trailing edge. Since the trailing-edge surface varies for different crack sizes, an offset wall-normal coordinate system $x'o'y'$ was

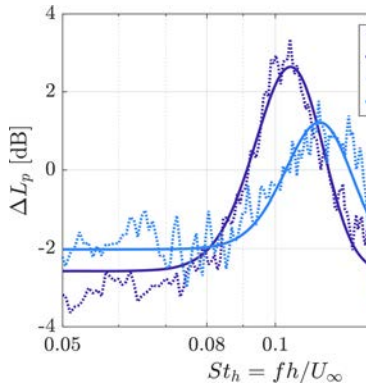


FIG. 3. The measured spectra and the fitted curves of $\Delta L_p$ for $W = 2.0$ mm case at zero angle of attack and 35 m/s inflow velocity for clean and turbulent inflow conditions.

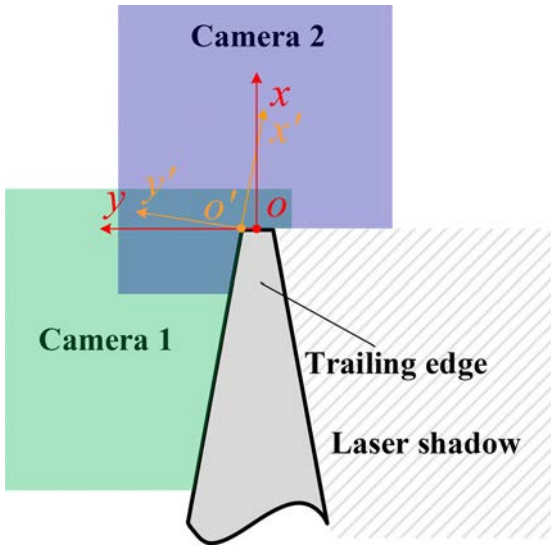


FIG. 4. Fields of view for the two cameras and the reference coordinate systems.

adopted to plot the boundary layer profiles, as shown in Fig. 4. The exposure time for each frame was 10 μs and the double shutter time was configured differently, which leads to approximately the same particle displacement in the free stream of 210 μm (16.8 pixels) for different inflow velocities; statistics were computed by recording 300 pairs of images.

The velocity field calculation was carried out using the software LaVision DaVis 10.2. To mitigate the effect of spurious reflections due to the airfoil solid wall, a background image, calculated by averaging all images, was subtracted from the raw images. A geometric mask for the airfoil and the laser shadow regions was added to remove the effects of reflections on the cross-correlation. A standard multi-pass 2D cross-correlation algorithm was performed for the vector calculation. Two initial passes and two final passes were applied with deformable windows; the sizes of the windows are $128 \times 128$ pixels and $24 \times 24$ pixels, respectively, and the window overlaps are 50% and 75%, respectively. This provides a spatial resolution of 0.3 mm and a vector spacing of 0.075 mm. The uncertainty of the mean velocity is estimated as $\varepsilon_U = \sigma_U/\sqrt{N}$ and the uncertainty of the root mean square velocity is estimated as $\varepsilon_{u'} = \sigma_U/\sqrt{2(N-1)}$,[57] where $\sigma_U$ is the maximum magnitude of the velocity fluctuations normalized by the inflow velocity ($\sigma_U = 20\%$ in the boundary layer in this study), and $N$ is the number of paired snapshots ($N = 300$ in this study). This yields an uncertainty of the mean velocity and root mean square velocity of 1.15% and 0.82%, respectively.

## III. RESULTS AND DISCUSSION

### A. Velocity field near the trailing edge

Figure 5 shows the mean flow velocity field near the trailing edge for the different damage cases for both clean and turbulent ($I = 4.0\%$) inflow conditions and the airfoil set at zero angle of attack. For the clean inflow condition (top row in Fig. 5), the contour lines of the velocity magnitude, $U$, normalized by the free-stream velocity, $U_\infty$, show that near the trailing edge, when increasing the size of the damage, the boundary layer is affected because of a different pressure gradient imposed by the variation in the geometry. For example, the space between the trailing-edge surface and the $0.4U_\infty$ contour line decreases as the damage size increases, which indicates that the velocity gradient near the surface is larger when the damage is larger. A similar trend of the velocity gradient can be observed near the airfoil surface when the inflow is turbulent, as shown in the bottom row in Fig. 5.

#### 1. Boundary layer profile of the mean velocity

The vortex shedding from a bluff body is affected by the velocity gradient of the boundary layer close to the location where the vortices are shed from the body.[37,38] Figure 6 shows the boundary layer profiles of velocity magnitude, $U$, sampled along the $y'$-axis, shown in the $x'o'y'$ reference system in Fig. 4, at the trailing edge for all the cases investigated, where the velocity is normalized by the boundary layer edge velocity, $U_e$. Figure 7 shows the corresponding velocity gradients, where the $y'$ axis is normalized by the boundary layer thickness $\delta$. In

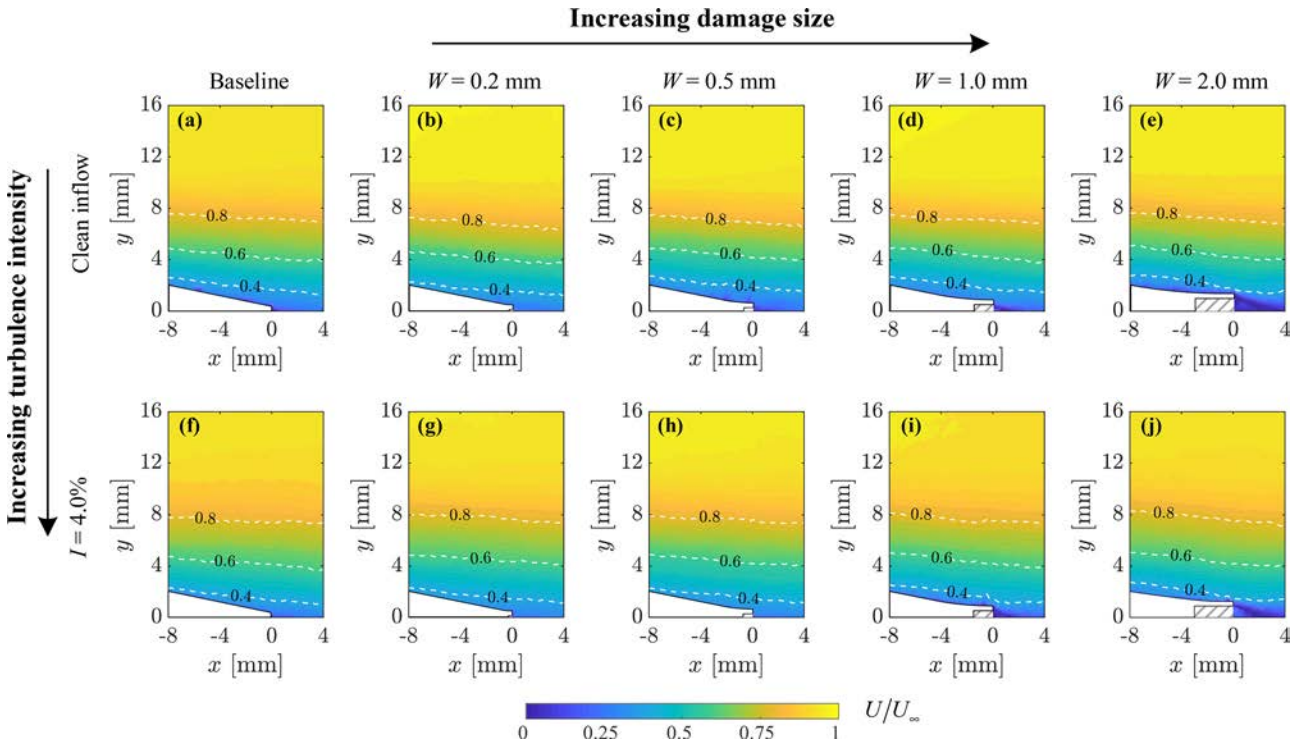


**FIG. 5.** Mean velocity field near the trailing-edge surface for different crack sizes with clean and turbulent inflows: (a)–(e) for clean inflow cases and (f)–(j) for turbulent inflow cases. The white blocks are half sections of the trailing edge and the shaded regions are the shadow areas of the laser.

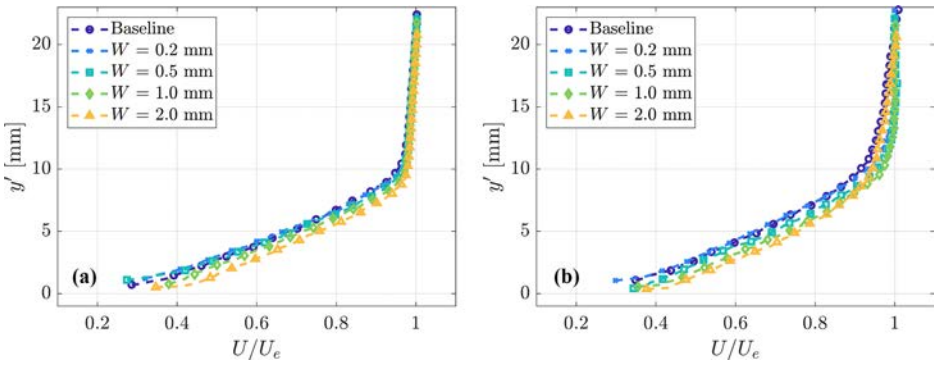


**FIG. 6.** Velocity profiles at the trailing edge for different crack sizes for (a) clean inflow and (b) turbulent inflow ($I = 4\%$) conditions.

the present work, the boundary layer thickness is defined as the point where the velocity within the boundary layer reaches 95% of $U_e$, i.e., $\delta = \delta_{95}$. To mitigate the impact of numerical differentiation, when directly calculating the gradient, a second-order regression with a window size of five points is applied to the velocity fields to calculate the derivative. In the figures, the markers indicate the data points at ten times the spacing of the original resolution, i.e., 0.75 mm, for clarity. The airfoil is tripped so the boundary layer is turbulent for all the cases. The figures confirm the qualitative observations reported previously: the velocity gradient within the inner region in the $y'$-axis direction increases with the increasing size of the damage. This is found for both inflow conditions. However, for the turbulent inflow cases, the velocity profile slopes ($\partial y'/\partial U$, reciprocal of gradient) at the boundary layer edge region for the baseline and $W = 2.0$ mm cases are smaller than the $W = 0.2$, 0.5, and 1.0 mm ones, which is also reflected in the gradient plots showing slightly larger values at the boundary layer edge.

Since the boundary layer data at the very near-wall region are not available, to quantify the boundary layer properties, the Clauser plot method[20,57,58] is employed. The turbulent boundary layer within the logarithmic region can be fitted as

$$U^+ = \frac{1}{\kappa}\ln y^+ + B, \tag{3}$$

where $\kappa = 0.41$ is the von Kármán constant and $B = 5$ as suggested in Refs. 57, 59, and 60. $U^+ = U/U_\tau$ and $y^+ = y'U_\tau/\nu$ are the nondimensional velocity and distance in the $y'$-axis direction relative to the wall (wall-normal), respectively, where $U_\tau$ is the friction velocity and $\nu$ is the kinematic viscosity. By introducing the skin friction coefficient, $C_f$, where

$$\frac{U_\tau}{U_e} = \sqrt{\frac{1}{2C_f}}, \tag{4}$$

and substituting it into Eq. (3), there is only one unknown variable $C_f$ that needs to be determined by fitting the log-law using boundary layer data within the logarithmic region, as shown in Fig. 8 for both the clean and turbulent inflow cases. In this study, data are selected within the range $30 < y^+ < 100$ for fitting to avoid the influence of near-wall unreliable measurements and outer-layer turbulence and wake effects. Within this range, the data points exhibit an approximately linear trend in a logarithmic-scale plot, corresponding to the best agreement with the log-law region of the boundary layer. Retrieving $U_\tau$, the boundary layer profile at the near-wall region (viscous sublayer) becomes

$$U^+ = y^+. \tag{5}$$

It should be noted that the fitting is performed under the zero-pressure-gradient (ZPG) assumption. However, for airfoil flows, pressure gradients are typically present, though they are usually weak at low angles of attack. As a result, the wall shear layer parameters may be slightly influenced by these unaccounted pressure gradients.

The friction coefficients, $C_f$, and friction velocities, $U_\tau$, together with their ratios to the baseline (subscript 0) for the above cases investigated are presented in Table II. The obtained $C_f$ and $U_\tau$ of the baseline case agree with the ones in previous studies.[16,20] For the clean inflows, as the crack size increases, the friction coefficient, $C_f$, and friction velocity, $U_\tau$, increase as well. This indicates that in the near-wall region, a greater trailing-edge crack size also leads to a larger velocity

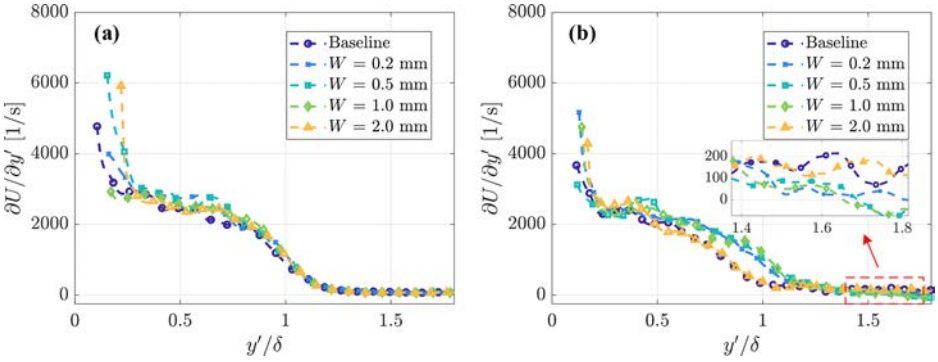


**FIG. 7.** Velocity gradient at the trailing edge for different crack sizes for (a) clean inflow and (b) turbulent inflow ($I = 4\%$) conditions.

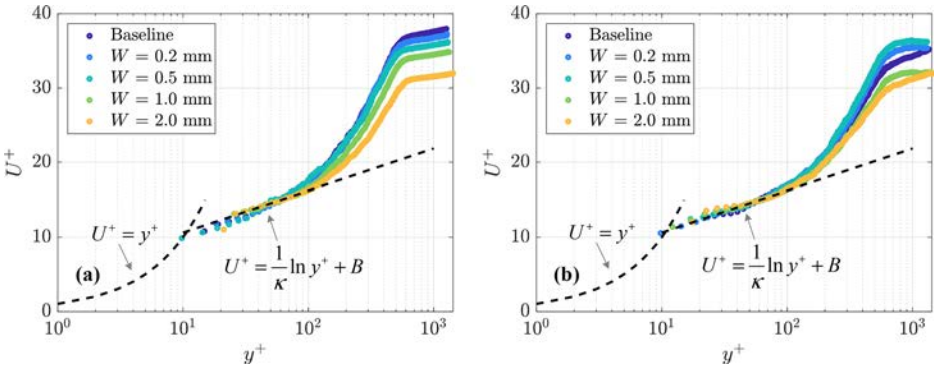


**FIG. 8.** The nondimensional velocity profiles at the trailing edge for different damage cases for (a) clean inflow and (b) turbulent inflow ($I = 4\%$) conditions.

**TABLE II.** Skin friction coefficient, $C_f$, and the friction velocity, $U_\tau$, obtained by applying Clauser's method.

| | Clean inflow | | | | $I = 4.0\%$ | | | |
|---|---|---|---|---|---|---|---|---|
| Crack size, $W$ (mm) | $C_f(\times 10^{-3})$ | $C_f/C_{f,0}$ | $U_\tau$ (m/s) | $U_\tau/U_{\tau,0}$ | $C_f(\times 10^{-3})$ | $C_f/C_{f,0}$ | $U_\tau$ (m/s) | $U_\tau/U_{\tau,0}$ |
| 0 (Baseline) | 1.4 | 1.000 | 0.887 | 1.000 | 1.6 | 1.000 | 0.960 | 1.000 |
| 0.2 | 1.5 | 1.071 | 0.918 | 1.035 | 1.6 | 1.000 | 0.940 | 0.979 |
| 0.5 | 1.5 | 1.071 | 0.944 | 1.064 | 1.5 | 0.938 | 0.917 | 0.955 |
| 1.0 | 1.7 | 1.214 | 0.977 | 1.102 | 1.9 | 1.188 | 1.024 | 1.067 |
| 2.0 | 2.0 | 1.429 | 1.068 | 1.204 | 2.0 | 1.250 | 1.058 | 1.102 |

gradient. Similarly to the clean inflow cases, when the turbulent inflow is investigated, both the friction coefficient, $C_f$, and friction velocity, $U_\tau$, tend to be greater but the differences between the smaller crack cases are not significant. For a given trailing-edge geometry, the skin friction coefficient and skin friction velocity are weakly affected by the presence of the turbulent inflow. Similar findings have been reported in the literature; the insignificance of these variations was attributed to the low turbulence intensity and small integral length scale of the free-stream turbulence.[39,42]

Figures 9 and 10 show the mean velocity profiles and gradients for the baseline airfoil and the ones with a crack of $W = 2.0$ mm for clean inflow conditions at different free-stream velocities. With the increase in inflow velocity, for both baseline and cracked cases, the differences in velocity profiles are mainly observed in the inner region. The velocity gradient in this region is greater as the inflow velocity increases. This agrees with the trend of boundary development on a flat plate or in a pipe by increasing the Reynolds number.[61] Similarly, by comparing the cracked cases to the baseline for all the tested velocities, it is found that the cracks lead to a greater velocity gradient within the inner region of the boundary layer, which agrees with the results discussed earlier in this paper. Figures 11 and 12 show the same cases for the turbulent inflow condition, demonstrating that the cracks lead to similar changes in the boundary layer velocity gradient. However, by changing the inflow conditions, as shown in Figs. 9 and 11, the velocity gradient at the boundary layer edge is greater for the turbulent condition, as the slopes of the velocity profiles in the region near the boundary layer edge are smaller than those tested with clean inflow. This suggests that the inflow turbulence strongly affects the boundary layer at the outer region. Similar results were also found in previous works.[62–64]

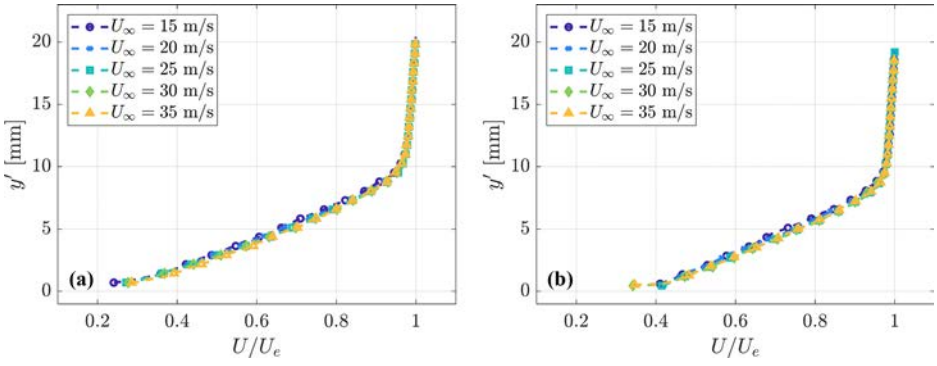


**FIG. 9.** Velocity profiles at the trailing edge for clean inflows of different mean velocities: (a) baseline and (b) $W = 2.0$ mm.

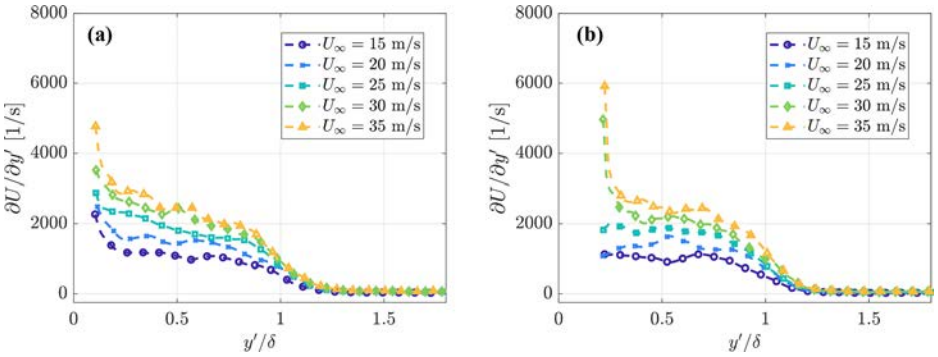


**FIG. 10.** Velocity gradients at the trailing edge for clean inflows of different mean velocities: (a) baseline and (b) $W = 2.0$ mm.

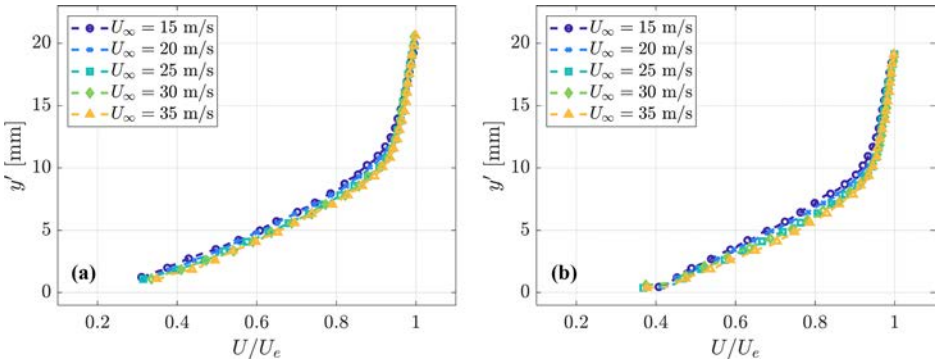


**FIG. 11.** Velocity profiles at the trailing edge for turbulent inflows of different mean velocities: (a) baseline and (b) $W = 2.0$ mm.

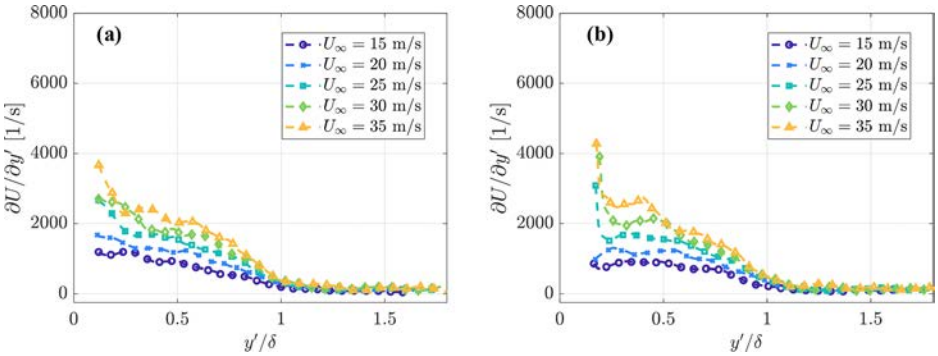


**FIG. 12.** Velocity gradients at the trailing edge for turbulent inflows of different mean velocities: (a) baseline and (b) $W = 2.0$ mm.

Figures 13 and 14 show the mean velocity profiles and gradients of the baseline and $W = 2.0$ mm cases at angles of attack of 0° and 5° for the clean inflow condition. On the suction side, as the angle of attack increases, the velocity gradient becomes smaller in the inner region of the boundary layer, where the slope of the velocity profile is greater, for both the baseline and damaged cases; this agrees with the results of previous studies in the literature.[65] As the crack is present, for both angles of attack, the velocity gradient on the suction side becomes slightly greater compared with the baseline case. On the pressure side, the increase in the angle of attack leads to a greater velocity gradient near the wall for both the baseline and cracked cases; however, as the angle of attack increases, the differences in the boundary layer between the baseline and the cracked case become less significant. Figures 15 and 16 show the same cases for the turbulent inflow condition, where similar results can be observed. The differences happen at the edge of the boundary layer, where for the turbulent inflow cases, the slopes of the boundary layer profiles become smaller indicating greater velocity gradients compared with the same cases for the clean inflow.

Previous results at zero angle of attack indicated that both surface geometry and inflow turbulence influence the boundary layer development and its velocity profile. As the angle of attack increases, the boundary layer on the suction side visibly thickens, while it thins on the pressure side, as shown in Figs. 13 and 15. To further examine the influence of the crack and inflow turbulence on the boundary layer, both for the baseline and $W = 2.0$ mm cracked configurations, the nondimensional velocity profiles on the suction and pressure sides are shown in Figs. 17 and 18, with corresponding skin friction coefficients, $C_f$, and friction velocities, $U_\tau$, listed in Table III.

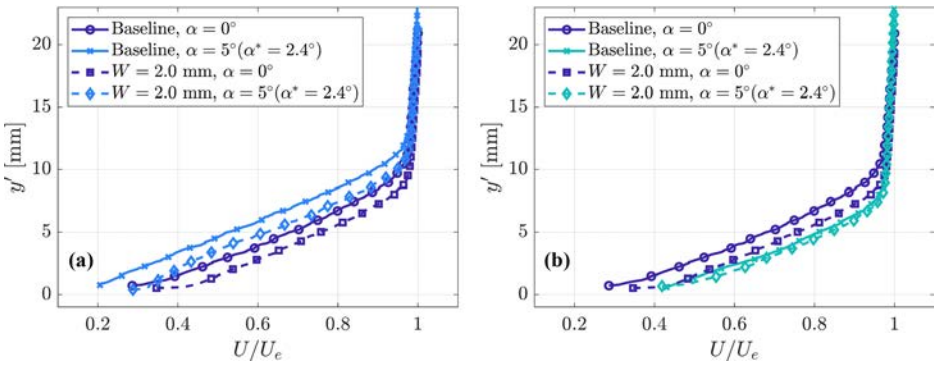


**FIG. 13.** Velocity profiles at the trailing edge of the clean inflow condition for different angles of attack: (a) on the suction side and (b) on the pressure side.

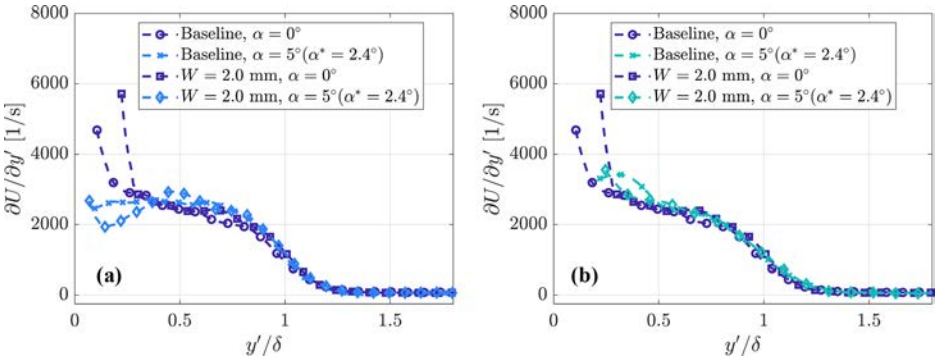


**FIG. 14.** Velocity gradients at the trailing edge of the clean inflow condition for different angles of attack: (a) on the suction side and (b) on the pressure side.

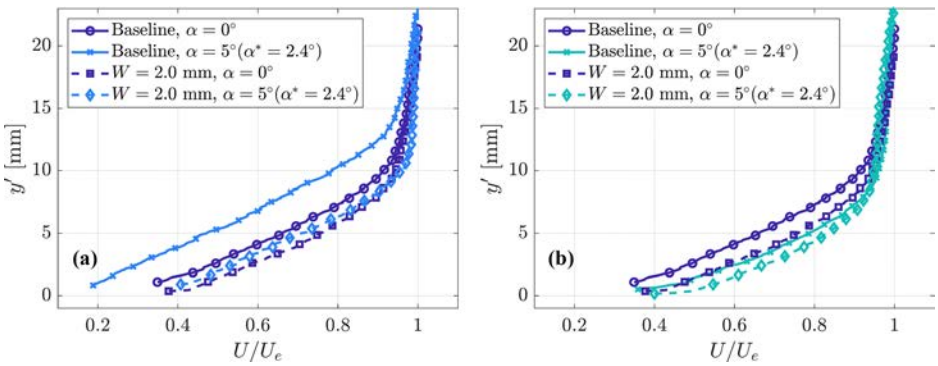


**FIG. 15.** Velocity profiles at the trailing edge of the turbulent inflow condition ($I = 4.0\%$) for different angles of attack: (a) on the suction side and (b) on the pressure side.

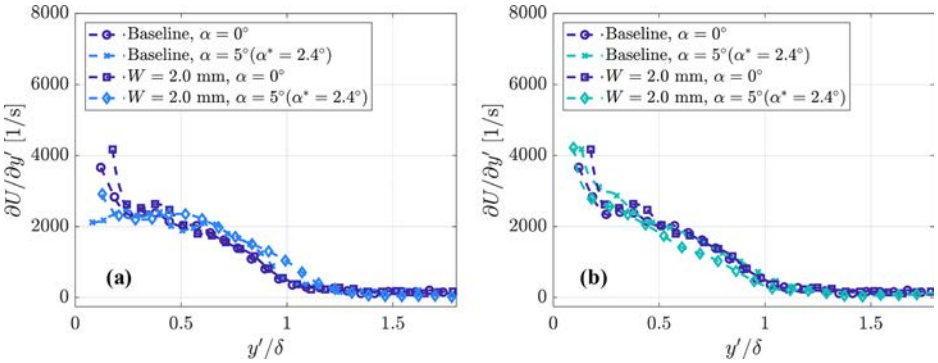


**FIG. 16.** Velocity gradients at the trailing edge of the turbulent inflow condition ($I = 4.0\%$) for different angles of attack: (a) on the suction side and (b) on the pressure side.

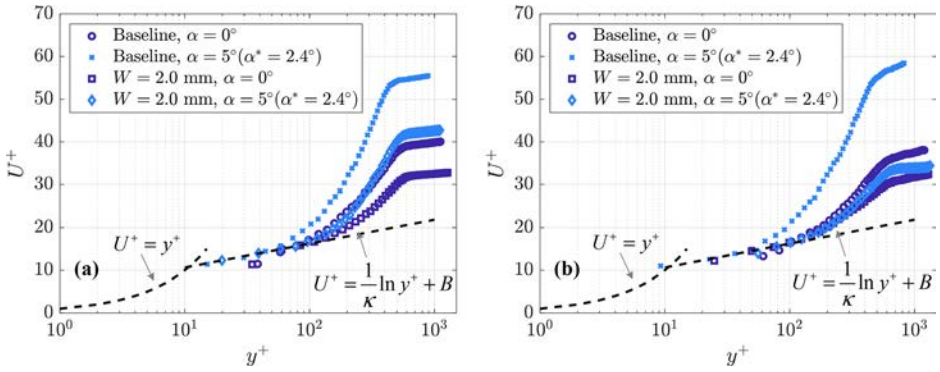


**FIG. 17.** The nondimensional velocity profiles at the trailing edge on the suction side for (a) clean inflow and (b) turbulent inflow ($I = 4\%$) conditions.

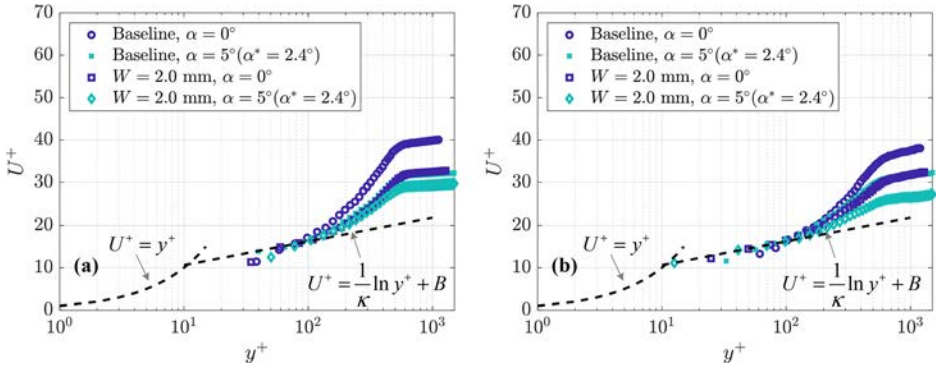


**FIG. 18.** The nondimensional velocity profiles at the trailing edge on the pressure side for (a) clean inflow and (b) turbulent inflow ($I = 4\%$) conditions.

**TABLE III.** Skin friction coefficient, $C_f$, and the friction velocity, $U_\tau$, for cases at $\alpha = 5°$.

| | Clean inflow | | | | I = 4.0 % | | | |
|---|---|---|---|---|---|---|---|---|
| Crack size, $W$ (mm) | $C_f(\times 10^{-3})$ | $C_f/C_{f,0}$ | $U_\tau$ (m/s) | $U_\tau/U_{\tau,0}$ | $C_f(\times 10^{-3})$ | $C_f/C_{f,0}$ | $U_\tau$ (m/s) | $U_\tau/U_{\tau,0}$ |
| Suction side | | | | | | | | |
| 0 (Baseline) | 0.65 | 1.000 | 0.614 | 1.000 | 0.59 | 1.000 | 0.572 | 1.000 |
| 2.0 | 1.1 | 1.692 | 0.805 | 1.311 | 1.7 | 2.881 | 0.961 | 1.680 |
| Pressure side | | | | | | | | |
| 0 (Baseline) | 1.9 | 1.000 | 1.059 | 1.000 | 1.9 | 1.000 | 1.001 | 1.000 |
| 2.0 | 2.2 | 1.158 | 1.146 | 1.082 | 2.6 | 1.368 | 1.200 | 1.199 |

For the baseline case at $\alpha = 5°$, only minor differences in $C_f$ and $U_\tau$ are observed between the clean and turbulent inflows on both sides. However, on the suction side, both $C_f$ and $U_\tau$ are lower than those for the same configuration at zero angle of attack. In contrast, for the case with a $W = 2.0$ mm trailing-edge crack, as shown in Figs. 13 and 15, the altered geometry shows a thinner boundary layer near the trailing edge for both clean and turbulent inflow cases and both $C_f$ and $U_\tau$ increase with respect to the baseline case. Notably, unlike the zero angle-of-attack case, the presence of inflow turbulence in the 2.0 mm cracked configuration further increases $C_f$ and $U_\tau$. On the pressure side, both $C_f$ and $U_\tau$ show an overall increase for the baseline and cracked configurations when compared to the zero angle-of-attack cases; for the 2.0 mm crack case in particular, $C_f$ and $U_\tau$ increase in the presence of inflow turbulence, which is consistent with the behavior observed on the suction side.

### 2. Boundary layer thickness and displacement thickness

Figure 19 shows the boundary layer thickness, $\delta$, and displacement thickness, $\delta^*$, at the trailing edge for the cases with different crack sizes and the corresponding ratios normalized by the baseline configuration. The displacement thickness is defined as $\delta^* = \int_0^\delta (1 - U(y')/U_e)\mathrm{d}y'$. When the inflow is clean, both the boundary layer thickness and displacement thickness tend to decrease as the crack size increases. This is because the crack results in an increase in the velocity gradient of the boundary layer at the trailing edge, and as the size of the crack increases, the velocity gradient becomes greater. When the turbulent inflow is introduced, both the boundary layer thickness and displacement thickness tend to be thicker compared with those for the clean inflow condition. For the damaged cases with smaller cracks

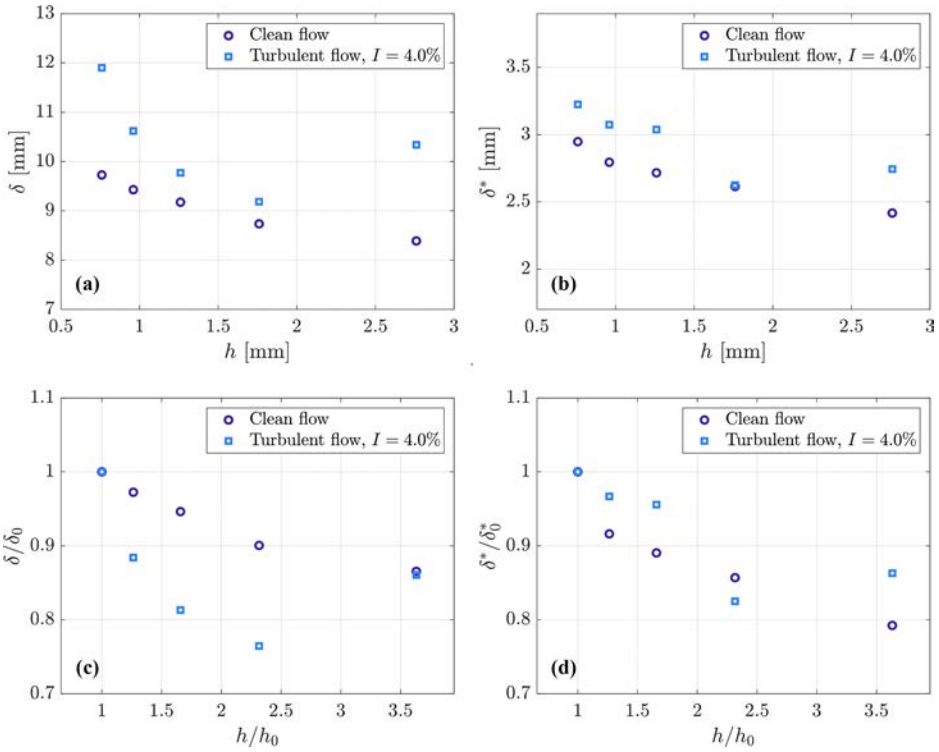


**FIG. 19.** Boundary layer thickness and displacement thickness at the trailing edge for different crack sizes for 35 m/s inflow and zero angle-of-attack condition: (a) boundary layer thickness; (b) displacement thickness; (c) and (d) the corresponding normalized values with the baseline.

($W = 0.2$, 0.5, and 1.0 mm), a decay trend can be seen both for the boundary layer thickness and displacement thickness. However, for the 2.0 mm crack case, an increasing trend is presented for both boundary layer thickness and displacement thickness. This mainly results from a lower slope of the velocity profile for the 2.0 mm crack case near the boundary layer edge where the velocity recovers to the free-stream velocity more slowly compared to the other cracked cases, as shown in Fig. 6(b).

Varying the inflow velocity (as well as the chord-length-based Reynolds number), as shown in Fig. 20 for the crack where $W = 2.0$ mm, both boundary layer thickness and displacement thickness become thinner as the inflow velocity increases. For the turbulent inflow condition, both the boundary layer and displacement thickness become slightly thicker than the clean inflow ones. This is attributed to greater gradients (with smaller slopes of velocity profiles) near the edge of the boundary layer when the inflow is turbulent, thus making a greater integral area below the velocity profile for the calculation of displacement thickness, as discussed previously when comparing Figs. 9 and 11. For both clean and turbulent inflow conditions, the measured boundary layer thickness or displacement thickness decays with the $-1/5$th power law of the chord-length-based Reynolds number, which agrees with the trends of turbulent boundary layer thickness or displacement thickness for a flat plate as the Reynolds number increases.[66] Although the same power law applies and the boundary layer thickness ratio, $\delta/\delta_0$, normalized with the baseline shows only a slight difference between clean and turbulent inflow conditions (0.85–0.89), as shown in Figs. 15(c) and 15(d), the displacement thickness ratio, $\delta^*/\delta_0^*$, exhibits a more noticeable difference, increasing from approximately 0.8 under clean inflow to 0.85–0.90 under turbulent inflow.

## B. Velocity field of the near wake

In Sec. III A, the boundary layer properties in the presence of cracks and inflow turbulence were discussed. However, it is still not clear how the induced changes in boundary layers and inflow conditions alter the coherent vortex shedding in the near wake, which is directly associated with the tones in the trailing-edge noise. Therefore, to analyze the relevant coherent vortex shedding and eventually interpret the physics of the noise changes, proper orthogonal decomposition (POD)[53,54] is performed in the near wake to filter the dominant coherent vortex structures. For a description of the POD approach adopted, the reader can refer to Refs. 53 and 54.

Figure 21 shows the energy distribution of POD modes, $\phi_v$, for the vertical component of the velocity, $v$, for the crack sizes equal to 1.0 and 2.0 mm with both clean and turbulent inflows. The energy of each $i$-th POD mode, $\lambda_i$, is scaled by the total energy of all modes. When the inflow is clean, both for the 1.0 mm and the 2.0 mm cracks, the energy of the first two modes is close, after which a clear step change appears in the higher-order modes. This indicates that the first two modes might be associated with strong coherent vortex structures in the near wake.[54] As the damage level increases, the energy of the first two modes increases which suggests that the contribution of coherent vortex structures to the total fluctuations in the near wake is greater.[67,68] When the inflow is turbulent, for the 2.0 mm crack, the difference in the energy between the first two modes becomes larger compared to the clean inflow case and the step change of the energy distribution is not evident. To verify whether the first two modes for this case are associated with the same coherent vortex shedding, an analysis for the spatial distribution of the vortex structures in the first two modes is conducted subsequently, as suggested in the Refs. 67 and 69.

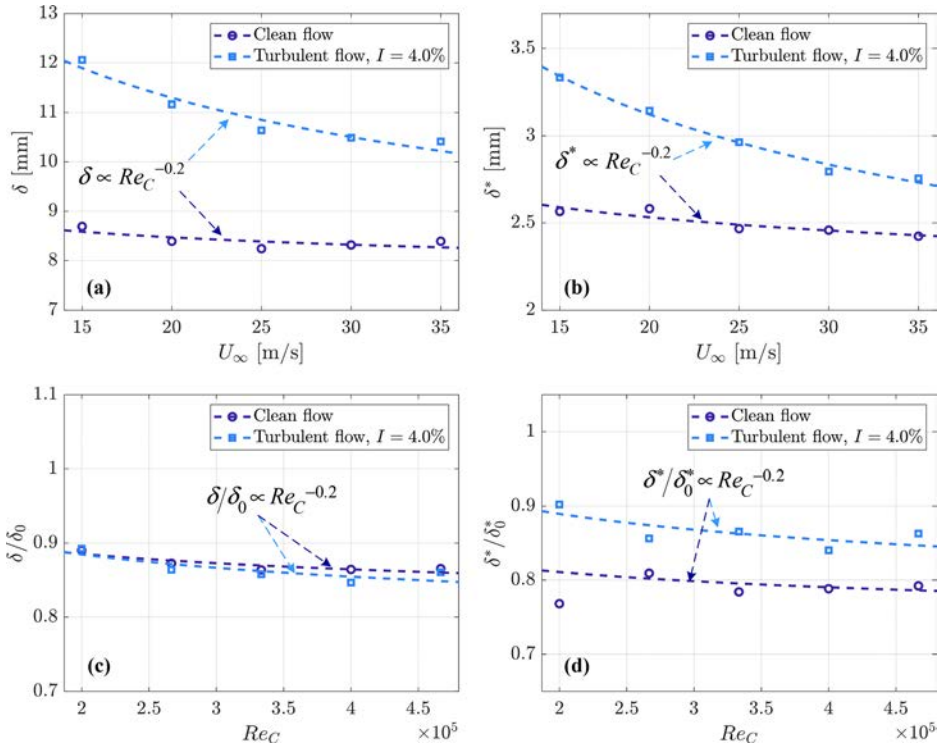


**FIG. 20.** Boundary layer thickness and displacement thickness at the trailing edge with $W = 2.0$ mm for different inflow velocities and zero angle-of-attack conditions: (a) boundary layer thickness; (b) displacement thickness; (c) and (d) the corresponding normalized values with the baseline against chord-length-based Reynolds number.

Figure 22 shows the first two POD modes for the same cases mentioned above. The $x$ axis and $y$ axis are scaled with the trailing-edge thickness, which allows a comparison of the relative size of the vortices. For all the cases, it is observed that there is a difference between the locations of the vortex structure cores in the first mode and second mode, with the latter being located at a distance of approximately 1/4 of the length of the vortex structures downstream.[54,67,68,70,71] This confirms that the first two modes are linked to the same coherent vortex shedding. Comparing the 1.0 mm crack case with the 2.0 mm crack case for the clean inflow condition, it can be observed that the vortex structures are stronger for the latter case, as expected, because a thicker trailing edge leads to a greater velocity gradient discussed in Sec. III A 1. For the turbulent inflow condition, the shapes of the first two modes look like the ones for the clean inflow condition but the strength and size of the vortex structures appear to be slightly lower. This agrees with the findings in the previous work on the vortex shedding from a cylinder in the presence of free-stream turbulence.[47–49] Therefore, despite the absence of a step-like energy distribution, the POD modes seem to be representative of coherent vortex shedding also in this case. The reasons for such a discrepancy in the mode energy distribution are not yet clear and will require further analysis.

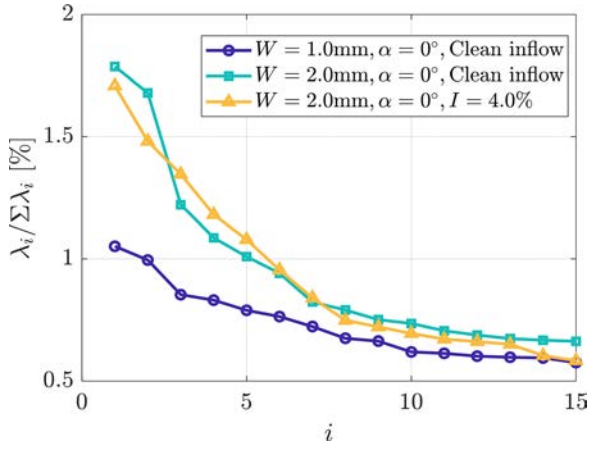


**FIG. 21.** The energy distribution of the POD modes for 1.0 mm crack and 2.0 mm crack cases for different inflow conditions.

Figure 23(a) shows the energy distribution of the POD modes for the 2.0 mm crack case at an angle of attack of $\alpha = 5°$ ($\alpha^* = 2.4°$) and the clean inflow condition. In contrast to the case at zero angle of attack, the energy of the first mode is much larger than the second mode and the step change is more visible after modes 2 and 3. The energies of the second and third modes are close, and these two modes seem to be paired, thus hinting at coherent vortex shedding, while the first mode might indicate non-periodic large-scale structures shed because of localized flow separation near the trailing edge. Figures 23(b)–23(d) show the first three POD modes. The second and third modes show similar characteristics to the ones of the first two modes for the zero angle-of-attack case: the cores of the vortex structures in the second mode shift 1/4 of the length of the vortex structures downstream, which confirms that these two modes are associated with the same coherent vortex structures in the near wake.

Figure 24 shows the root mean square velocity fluctuations in the near wake reconstructed by the paired modes for the cases discussed above, which indicates the intensity of the coherent vortex structures

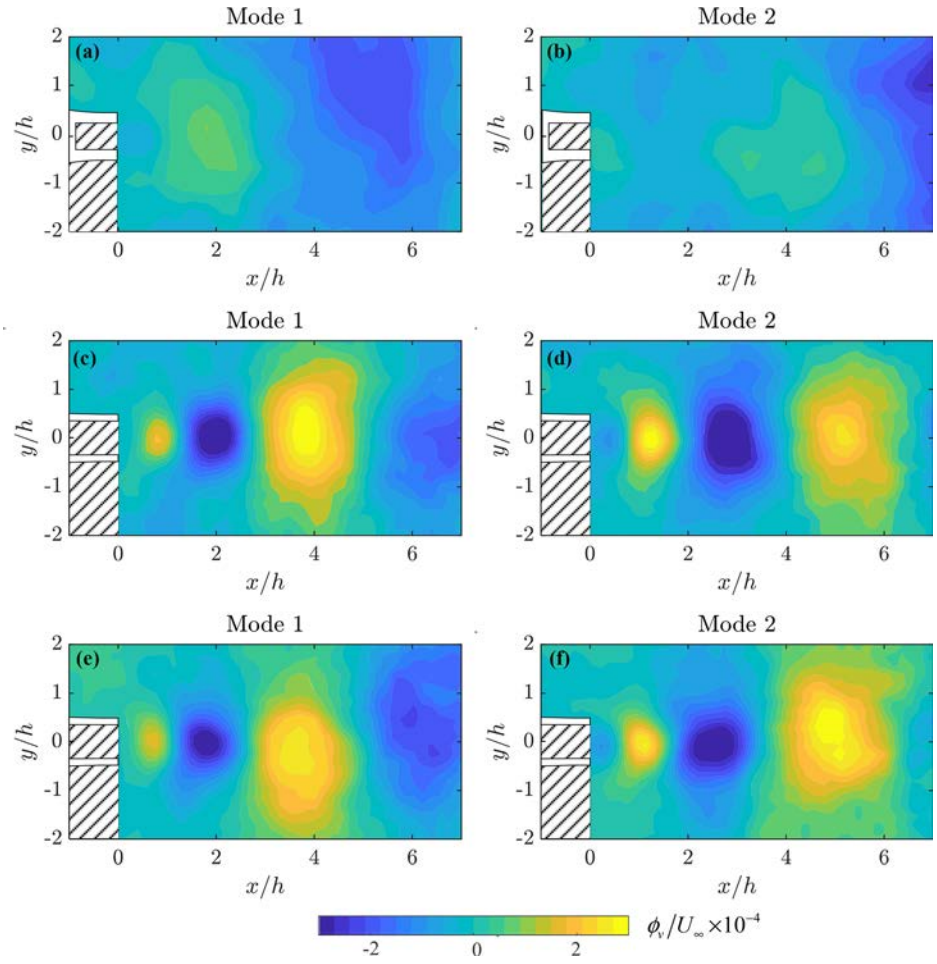


**FIG. 22.** First two POD modes of the *v* component for the cases: (a) and (b) 1.0 mm crack case for clean inflow condition; (c) and (d) 2.0 mm crack for clean inflow condition; (e) and (f) 2.0 mm crack for turbulent inflow condition. The white blocks are the trailing edges, and the shaded sections are the shadow areas of the laser.

in the near wake. As the crack increases to 2.0 mm, the strength of the coherent vortex structures increases significantly, which is reasonable because a greater velocity gradient is observed on the boundary layers. On the other hand, for the same crack size, the strength of the coherent vortex structures decreases as the inflow turbulence is present, which might be because the inflow turbulence disrupts the formation and evolution of shear layers accelerating vortex breakdown to smaller structures, thus reducing the coherence of vortex shedding.[47–49] As the angle of attack is increased, the strength of the coherent vortex structures decreases due to the asymmetry of the boundary layers on the suction and pressure sides.

In order to determine and compare the length scales, $\Lambda$, associated with the coherent vortex structures for different cases, a cross-correlation analysis[72] in the streamwise direction is performed for the paired POD modes of the vertical velocity component. As shown in Fig. 25(a), assuming there are two paired modes, $\phi_{v,1}(x,y)$ and $\phi_{v,2}(x,y)$, the cross-correlation coefficient of the two modes with a displacement, $\Delta x$, is calculated within the dashed region as

$$\sigma(\Delta x) = \frac{\sum \phi_{v,1}(x+\Delta x, y)\phi_{v,2}(x,y)}{|\phi_{v,1}(x+\Delta x, y)||\phi_{v,2}(x,y)|}. \quad (6)$$

Figure 25(b) shows the cross-correlation coefficients of the paired modes for the 1.0 and 2.0 mm damage cases for different test conditions. The displacement is scaled with the trailing-edge thickness, $h$. Due to the orthogonality of the POD modes, the cross-correlation coefficients for all the cases are all at zero when the displacement $\Delta x = 0$. The location of the first peak of cross-correlation coefficients indicates the 1/4 length of the coherent vortex structures, and the location of the first valley indicates the 3/4 length of the coherent vortex structures. The location of the first peak of the cross-correlation coefficients for the case with the 1.0 mm crack is at $\Delta x/h = 2.6$, and it is greater than the one for the 2.0 mm crack cases at $\Delta x/h = 1.0$, which means the relative size of the coherent vortex structures is larger. However, for all the tested cases with a 2.0 mm crack, the locations of the first peak of the cross-correlation coefficients are close at $\Delta x/h = 1.0$, which makes it difficult to compare the sizes of vortex structures for these cases. The locations of the first valley for the 2.0 mm crack cases are at $\Delta x/h = 3.52$, 3.41, and 3.27 for the cases of clean inflow and zero angle of attack, turbulent inflow and zero angle of attack, clean inflow, and $\alpha = 5°$ ($\alpha^* = 2.4°$), respectively. This suggests the length scale of the coherent vortex structures for the first case is slightly greater than the ones of the other two cases.

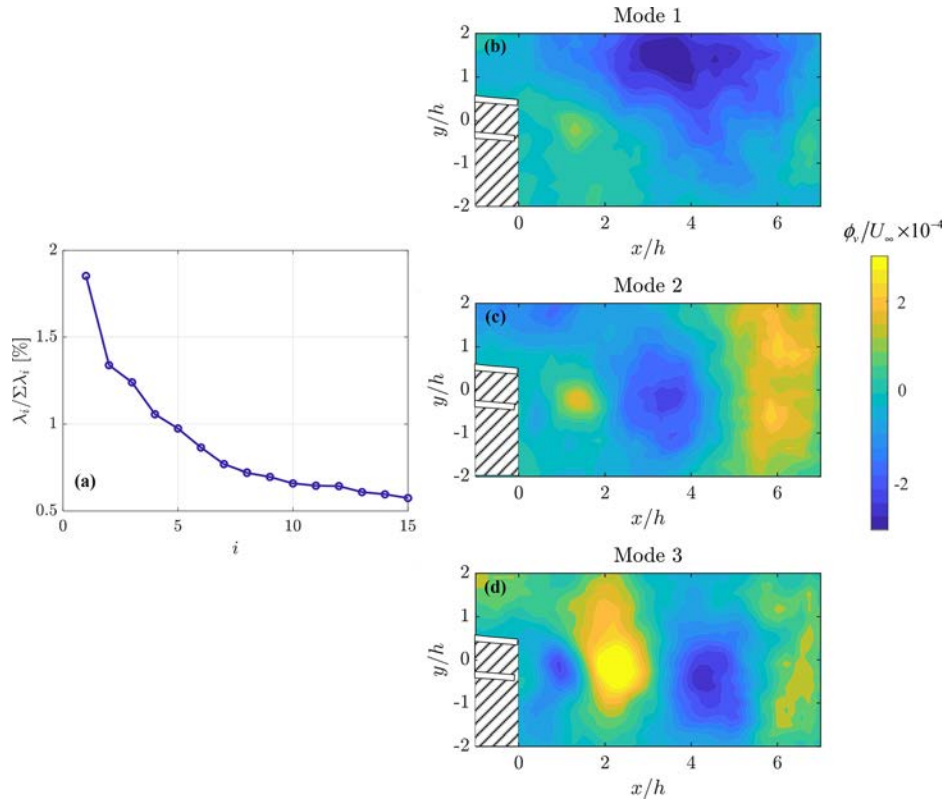


**FIG. 23.** The energy distribution and first three modes for the case with a 2.0 mm crack at $\alpha = 5^\circ$ ($\alpha^* = 2.4^\circ$) for the clean inflow condition. The white blocks are the trailing edges, and the shaded sections are the shadow areas of the laser.

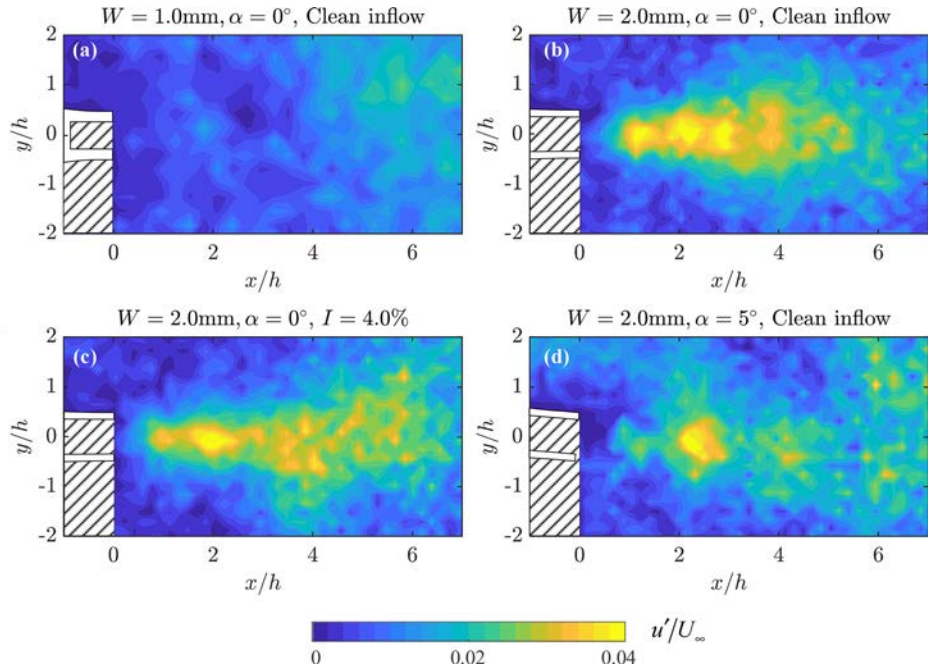


**FIG. 24.** The fluctuations in the near wake reconstructed with the paired modes: (a) for 1.0 mm crack case and (b)–(d) for 2.0 mm crack cases for different conditions. The white blocks are the trailing edge and the shaded sections are the shadow areas of the laser.

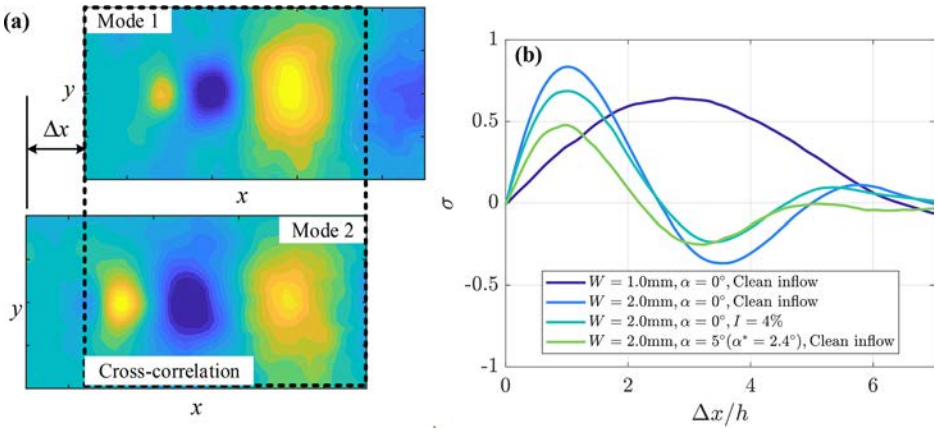


**FIG. 25.** Cross-correlation for the paired POD modes: (a) illustration for calculation and (b) results for different cases.

### C. Effects on the tones of trailing-edge noise

The preceding analysis and discussion explained in detail how trailing-edge crack and inflow turbulence alter the boundary layer properties and coherent vortex shedding at the trailing edge. This can further explain their influence on the shift of the tonal noise peak. Figure 26 shows the relative sound pressure level, $\Delta L_p = L_p - L_{p,\text{Baseline}}$ (where $L_p$ and $L_{p,\text{Baseline}}$ are the sound pressure levels for the cracked and baseline cases under the same test condition), and the corresponding fitted curves of the spectra for the representative cases with different crack sizes and inflow conditions. The frequency is scaled using the trailing-edge-thickness-based Strouhal number, $St_h = fh/U_\infty$. The detailed acoustic observations were reported in Ref. 25. The vortex shedding frequency depends on the convective velocity of vortex shedding and vortex length scale, i.e., $f = U_c/\Lambda$. Therefore, $St_h$ can be calculated as $St_h = \frac{U_c}{U_\infty}\frac{h}{\Lambda}$, which is proportional to the value of $h/\Lambda$, assuming that $U_c/U_\infty$ is a constant. The spectral peak for the case with the crack size of $W = 2.0$ mm is narrower with a higher $St_h$ at 0.1052 compared with the one for the damage case of $W = 1.0$ mm, which is at 0.085. This is because the strength of the coherent vortex structures is greater (as shown in Fig. 24) and the relative length scale, $\Lambda/h$, is shorter (as shown in Fig. 25) when the damage level increases as discussed above. Similarly, for the cases with a turbulent inflow or at a higher angle of attack, the intensity of the coherent vortex shedding is less and the vortex length scale, $\Lambda$, is shorter, which leads to a tone with lower amplitude and higher frequency in the spectrum. As the velocity increases, the amplitude of the tonal peak increases and the location of the tonal peak shifts to a higher value of $St_h$. This is attributed to a greater velocity gradient in the boundary layer and thus stronger coherent vortex structures with slightly shorter length scales in the near wake. A similar result was observed in some numerical and experimental studies,[73,74] where the ratio of the vortex structure length to trailing-edge thickness, $\Lambda/h$, slightly shifts to a higher value as the Reynolds number increases.

In order to investigate the influence of displacement thickness on the tonal noise frequency, as shown in Fig. 27, the spectra of relative sound pressure level are scaled using the displacement-thickness-based Strouhal number, $St_{\bar{\delta}^*}$(where $\bar{\delta}^* = (\delta_p^* + \delta_s^*)/2$ is the averaged boundary layer displacement thickness over the pressure and suction sides). For the clean inflow case, all the spectral peaks of $\Delta L_p$ collapse at $St_{\bar{\delta}^*} \sim 0.92$, indicating that the displacement thickness provides an effective scaling parameter for tonal noise frequency. In contrast, for the turbulent inflow cases, the spectral peaks no longer collapse and instead decrease from 0.135 to 0.115 with increasing inflow velocity (and thus the chord-length-based Reynolds number). This may be attributed to the inflow turbulence disrupting the formation and evolution of the wake vortex structures, as discussed previously, which weakens the scaling correlation between the displacement thickness and the coherent vortex shedding process. This suggests that the influence of inflow turbulence cannot be neglected when scaling trailing-edge noise based on boundary layer parameters.

As suggested by Brooks *et al.*,[36] the distribution of $St_{h,\text{peak}}$ as a function of $h/\bar{\delta}^*$, for $h/\bar{\delta}^* \geq 0.2$, follows the semi-empirical law

$$St_{h,\text{peak}} = \frac{0.212 - 0.0045\Psi}{1 + 0.235\left(h/\bar{\delta}*\right)^{-1} - 0.0132\left(h/\bar{\delta}*\right)^{-2}}, \quad (7)$$

where $\Psi$ is the solid angle (in degrees) between the sloping surfaces upstream of the trailing edge as defined in the reference paper and shown in the upper illustration of Fig. 28(a). In the present work, the solid angle is 21.22° for the baseline airfoil. As the crack is present, due to the change in geometry at the trailing edge, an equivalent solid angle is defined as shown in the lower illustration of Fig. 28(a). As the crack size increases, the effective solid angle slightly decreases and is estimated to be equal to 20.94°, 20.54°, 19.83°, and 18.44° for the four crack cases, 0.2, 0.5, 1.0, and 2.0 mm, respectively.

Figure 28(b) reports the measured $St_{h,\text{peak}}$, where the frequency of the tonal peak is determined using the fitting procedure shown in Fig. 26. As described above, the tonal peak cannot be accurately determined for all cases, and therefore, these points are excluded from the figure. The two solid lines in Fig. 28(b) are obtained by plotting the Strouhal number determined using Eq. (7) with solid angles equal to 18.44° (for $W = 2.0$ mm) and 21.22° (for the baseline case). Data for the clean inflow cases lie between the two lines, showing consistency with the model. It is interesting to note that as the crack size increases, the measured $St_{h,\text{peak}}$ is in agreement with the model. However, for the $W = 2.0$ mm case, the measured $St_{h,\text{peak}}$ values do not quite coincide with the upper line corresponding to the solid angle of 18.44°. This might be because the reduction in the effective solid angle as a function of the crack size is slightly overestimated in the lower illustration of Fig. 28(a).

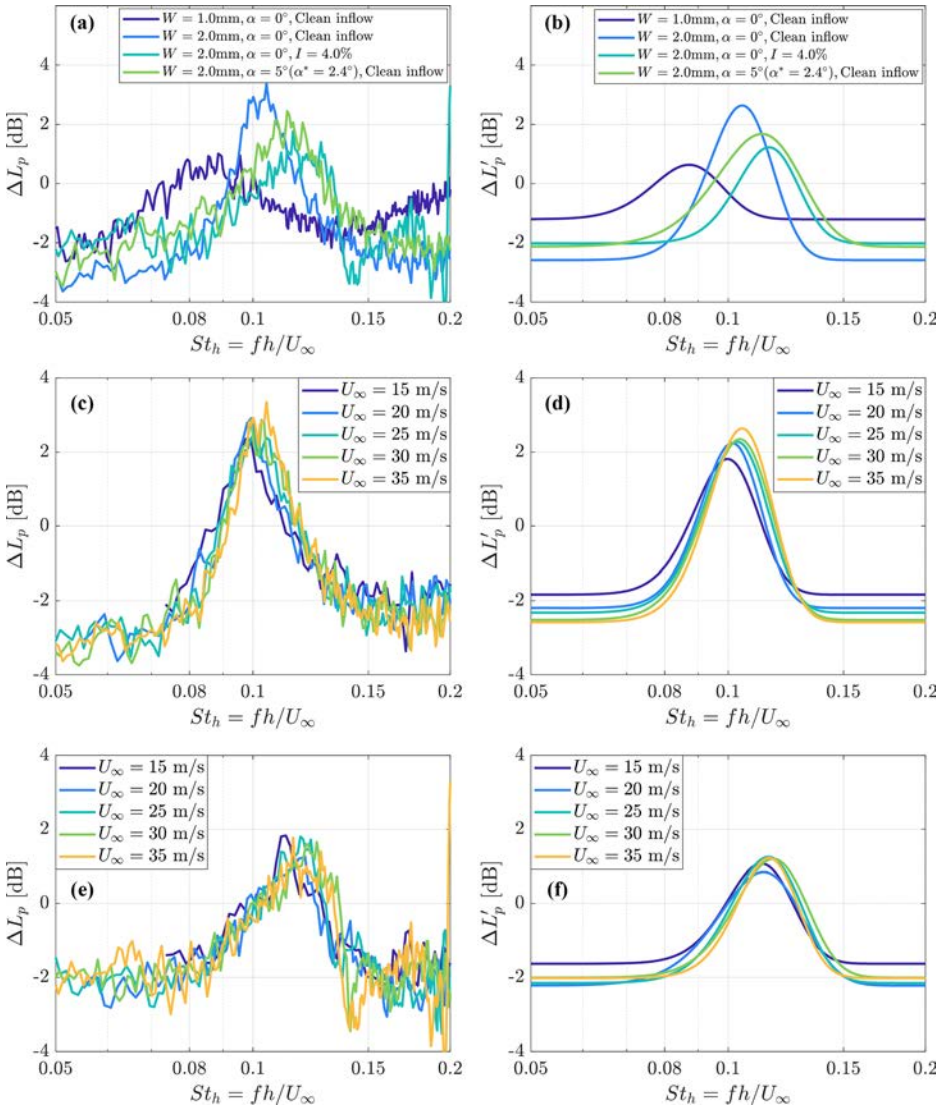


**FIG. 26.** Relative sound pressure level $\Delta L_p$ and the corresponding fitted curves for different cases: (a) under inflow velocity of $U_\infty = 35\,\text{m/s}$; (b) under inflow velocity of $U_\infty = 35\,\text{m/s}$ (fitted); (c) at different velocities with clean inflow; (d) at different velocities with clean inflow (fitted); at different velocities with turbulent inflow; and (e) at different velocities with turbulent inflow (fitted).

When the inflow is turbulent, the measured $St_{h,\text{peak}}$ shifts to higher values for all the investigated cases. This is because the inflow turbulence affects the boundary layer velocity profile, and the amplitude and frequency of the coherent vortex shedding as discussed previously. Although there is an offset with respect to the data for the clean inflow cases, the distribution of measured points for the turbulent inflow cases seems to follow the same trend line as for the clean inflow cases. This suggests that the model developed by Brooks *et al.*[36] can capture the variation in the Strouhal number as a function of crack size, albeit some correction is required for turbulent inflow. This result is significant because it suggests that the model could be used for practical applications. The exact correction will require further work.

## IV. CONCLUSIONS AND OUTLOOK

A study to investigate the relationship between the variations in the aerodynamic field and the far-field noise has been carried out on a NACA 0018 airfoil with simplified cracks of different sizes at the trailing edge. The airfoil self-noise was measured by a phased microphone array. With the help of beamforming and source power integration techniques, the contributions of the trailing-edge noise were obtained. The measurements for velocity fields near the surfaces of the trailing edge and the near wake were carried out using a PIV technique. A POD method was used to identify the dominant vortex structures from the velocity field data.

When the inflow is clean, the velocity gradient within the boundary layer increases as the crack size increases. As a result, the boundary layer thickness and displacement thickness decrease. When the inflow is turbulent, a similar trend of change in the boundary layer velocity profile in the inner region was observed with respect to the clean condition: as the damage level increases the velocity gradient in the boundary layer becomes greater. The difference from the clean cases is that at the edge of the boundary layer, the slope of the velocity profile

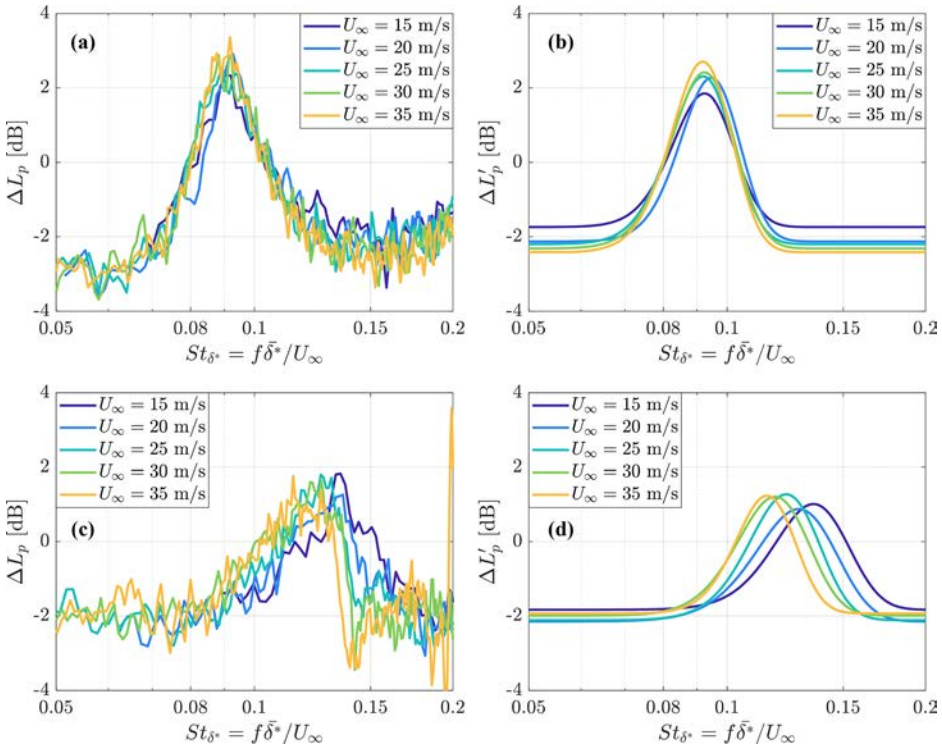


**FIG. 27.** Relative sound pressure level $\Delta L_p$ and the corresponding fitted curves normalized by the displacement thickness for the 2.0 mm crack case at different velocities: (a) and (b) with clean inflow; and (c) and (d) with turbulent inflow.

$(dy'/dU)$ decreases in the presence of turbulent inflow, and thus, a greater velocity gradient is present compared with the same case with clean inflow.

As the crack size increases, the coherent vortex structures in the near wake have greater intensities and shorter relative length scales $\Lambda/h$. This results in the shift of the tonal peak to a higher nondimensional frequency, $St_h$, with higher amplitude for a larger crack (with a blunter trailing edge). When the turbulent inflow is introduced, the shapes of coherent vortex structures in the near wake seem to be deformed with a slightly smaller size, which leads to the tonal peak slightly shifting to a higher value of $St_h$.

As expected, as the inflow velocity increases, for the same crack configuration, the boundary layer velocity gradient near the wall becomes greater for both clean and turbulent inflow conditions which leads to a thinner boundary layer thickness and displacement thickness. Also, when the airfoil is set at a higher angle of attack ($\alpha = 5°$, $\alpha^* = 2.4°$), the boundary layer velocity gradient becomes less on the suction side and greater on the pressure side, respectively, compared with the zero angle-of-attack case, which agrees with the findings in previous studies.[65] This also changes the formation of the coherent vortex shedding and thus the tone in the noise spectrum.

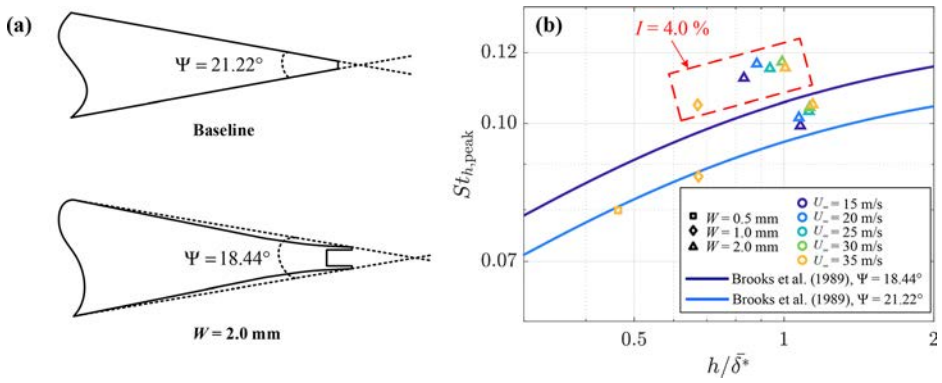


**FIG. 28.** Comparison with the model developed by Brooks *et al.*: (a) definition of solid angle for baseline and cracked cases; (b) dependence of the peak Strouhal number vs the ratio of trailing-edge thickness to boundary layer displacement thickness. The points outside the dashed box are for clean inflow cases. Solid lines are obtained using the semi-empirical law reported by Brooks *et al.* for the two different values of the solid angle shown in (a).

The current experimental data for both clean and turbulent inflow conditions fit well with the trend of the previous model found in Ref. 36 using the relationships between the $St_{h,\mathrm{peak}}$ and $h/\overline{\delta}^*$. This suggests that the model is still valid for the cases with a trailing-edge crack. However, when the inflow is turbulent, the frequencies of the tonal peaks shift to higher values. This suggests it is necessary to consider a correction term for the turbulent inflow conditions for the estimation of the crack size or trailing-edge thickness when using the current prediction models of the clean inflow version.

As can be seen from this study, the geometry of the trailing edge can alter the local boundary layer properties, vortex shedding, and consequent aerodynamic noise. This suggests that it may require a specific analysis for a certain type of damage. Accurately measuring the boundary layer properties of a rotating wind turbine blade is challenging in practice. However, a database of these properties can be readily obtained through a few experimental and numerical cases using interpolation methods or fast aerodynamic software, such as XFOIL,[75] for given operational conditions.

Although the experiments were performed for 2D airfoils, the noise generation mechanisms do not change when the blade is rotating.[76] The analytic and semi-empirical models of aerodynamic noise are still valid for a full-scale rotating wind turbine blade by accounting for the corrections of the Doppler effect and directivity terms.[36,77–79] Furthermore, the experiments were carried out in a controlled environment with mimicked inflow turbulence, which might be different from that in real wind farms. However, turbulence properties in a wind farm are often well characterized during both the pre-construction and post-construction phases, based on industry standards, historical measurements and simulations.[80,81] This allows direct use of available turbulence data without the need for extensive new measurements in many cases.

It should be noted that, in this study, the geometry of the trailing-edge crack is simplified and idealized. This is done to investigate the fundamental mechanisms in aerodynamics and aeroacoustics due to the presence of damage and inflow turbulence. In the real world, trailing-edge damage is diverse, leading to more complicated changes in shape at the trailing edge. Future work will aim to replicate realistic damage and validate the results in more representative conditions. Fatigue experiments are being conducted in laboratory environments on the scaled blades to create realistic damage. Based on these results, wind tunnel tests of a small-scale wind turbine will be performed, allowing for the investigation on the effects of damage under rotating conditions. Eventually, the approach will be validated in field tests on operational wind turbines, enabling direct comparison between damaged and undamaged blades under real operating conditions.

## ACKNOWLEDGMENTS

This work was supported by the China Scholarship Council (CSC) (Grant No. 201906330095).

## AUTHOR DECLARATIONS

### Conflict of Interest

The authors have no conflicts to disclose.

### Author Contributions

**Yanan Zhang:** Conceptualization (lead); Data curation (lead); Formal analysis (lead); Investigation (lead); Methodology (lead); Software (lead); Visualization (lead); Writing – original draft (lead). **Simon Watson:** Formal analysis (equal); Investigation (equal); Methodology (equal); Project administration (lead); Supervision (lead); Writing – review & editing (lead). **Daniele Ragni:** Data curation (equal); Investigation (supporting); Methodology (supporting); Resources (lead); Writing – review & editing (equal). **Francesco Avallone:** Conceptualization (lead); Data curation (lead); Formal analysis (equal); Investigation (lead); Methodology (lead); Supervision (lead); Validation (lead); Writing – review & editing (lead).

## DATA AVAILABILITY

The data that support the findings of this study are available from the corresponding author upon reasonable request.

## REFERENCES

[1]S. Watson, A. Moro, V. Reis, C. Baniotopoulos, S. Barth, G. Bartoli, F. Bauer, E. Boelman, D. Bosse, A. Cherubini, A. Croce, L. Fagiano, M. Fontana, A. Gambier, K. Gkoumas, C. Golightly, M. I. Latour, P. Jamieson, J. Kaldellis, A. Macdonald, J. Murphy, M. Muskulus, F. Petrini, L. Pigolotti, F. Rasmussen, P. Schild, R. Schmehl, N. Stavridou, J. Tande, N. Taylor, T. Telsnig, and R. Wiser, "Future emerging technologies in the wind power sector: A European perspective," Renewable Sustainable Energy Rev. **113**, 109270 (2019).
[2]D. Li, S. C. M. Ho, G. Song, L. Ren, and H. Li, "A review of damage detection methods for wind turbine blades," Smart Mater. Struct. **24**(3), 033001 (2015).
[3]F. Papi, L. Cappugi, S. Perez-Becker, and A. Bianchini, "Numerical modeling of the effects of leading-edge erosion and trailing-edge damage on wind turbine loads and performance," J. Eng. Gas Turbines Power **142**(11), 1–12 (2020).
[4]J. S. Chou, C. K. Chiu, I. K. Huang, and K. N. Chi, "Failure analysis of wind turbine blade under critical wind loads," Eng. Failire Anal. **27**, 99–118 (2013).
[5]Y. Ou, E. N. Chatzi, V. K. Dertimanis, and M. D. Spiridonakos, "Vibration-based experimental damage detection of a small-scale wind turbine blade," Struct. Health Monit. **16**(1), 79–96 (2017).
[6]A. Sarrafi, Z. Mao, C. Niezrecki, and P. Poozesh, "Vibration-based damage detection in wind turbine blades using phase-based motion estimation and motion magnification," J. Sound Vib. **421**, 300–318 (2018).
[7]B. Moynihan, B. Moaveni, S. Liberatore, and E. Hines, "Estimation of blade forces in wind turbines using blade root strain measurements with OpenFAST verification," Renewable Energy **184**, 662–676 (2022).
[8]D. Xu, P. F. Liu, and Z. P. Chen, "Damage mode identification and singular signal detection of composite wind turbine blade using acoustic emission," Compos. Struct. **255**, 112954 (2021).
[9]X. Y. Zhang, B. Zhou, H. Li, and W. Xin, "Depth detection of spar cap defects in large-scale wind turbine blades based on a 3D heat conduction model using step heating infrared thermography," Meas. Sci. Technol. **33**(5), 055008 (2022).
[10]S. Hwang, Y. K. An, J. Yang, and H. Sohn, "Remote inspection of internal delamination in wind turbine blades using continuous line laser scanning thermography," Int. J. Precis. Eng. Manuf.-Green Technol. **7**(3), 699–712 (2020).
[11]E. Nieuwenhuizen and M. Köhl, "Differences in noise regulations for wind turbines in four European countries," Euronoise **2015**, 333–338.
[12]T. Lutz, A. Herrig, W. Würz, M. Kamruzzaman, and E. Krämer, "Design and wind-tunnel verification of low-noise airfoils for wind turbines," AIAA J. **45**(4), 779–785 (2007).
[13]R. F. Jones, C. J. Doolan, and M. D. Teubner, "Minimization of trailing edge noise by parametric airfoil shape modifications," AIAA Paper No. 2011-2782, 2011.
[14]J. Gill, X. Zhang, and P. Joseph, "Symmetric airfoil geometry effects on leading edge noise," J. Acoust. Soc. Am. **134**(4), 2669–2680 (2013).
[15]F. Avallone, W. C. P. Van Der Velden, D. Ragni, and D. Casalino, "Noise reduction mechanisms of sawtooth and combed-sawtooth trailing-edge serrations," J. Fluid Mech. **848**, 560–591 (2018).
[16]L. T. Lima Pereira, D. Ragni, F. Avallone, and F. Scarano, "Aeroacoustics of sawtooth trailing-edge serrations under aerodynamic loading," J. Sound Vib. **537**, 117202 (2022).

[17]M. Herr and J. Reichenberger, "In search of airworthy trailing-edge noise reduction means," AIAA Paper No. 2011-2780, 2011.
[18]L. Rossian, R. Ewert, and J. W. Delfs, "Numerical investigation of porous materials for trailing edge noise reduction," Int. J. Aeroacoust. **19**(6–8), 347–364 (2020).
[19]C. Teruna, F. Avallone, D. Casalino, and D. Ragni, "Numerical investigation of leading edge noise reduction on a rod-airfoil configuration using porous materials and serrations," J. Sound Vib. **494**, 115880–115825 (2021).
[20]A. Rubio Carpio, R. Merino Martínez, F. Avallone, D. Ragni, M. Snellen, and S. van der Zwaag, "Experimental characterization of the turbulent boundary layer over a porous trailing edge for noise abatement," J. Sound Vib. **443**, 537–558 (2019).
[21]O. Ferret Gasch, S. Oerlemans, B. W. Faßmann, M. Herr, F. Bertagnolio, A. Fischer, B. Arnold, and T. Lutz, "Trailing edge noise prediction of wind turbine airfoils: A benchmark exercise," AIAA Paper No. 2019-2675, 2019.
[22]S. Luesutthiviboon, L. T. L. Pereira, D. Ragni, F. Avallone, and M. Snellen, "Aeroacoustic benchmarking of trailing-edge noise from NACA 633–018 airfoil with trailing-edge serrations," AIAA J. **61**(1), 329–354 (2023).
[23]B. Chen, S. Yu, Y. Yu, and Y. Zhou, "Acoustical damage detection of wind turbine blade using the improved incremental support vector data description," Renewable Energy **156**, 548–557 (2020).
[24]F. P. García Márquez, P. J. Bernalte Sánchez, and I. Segovia Ramírez, "Acoustic inspection system with unmanned aerial vehicles for wind turbines structure health monitoring," Struct. Health Monit. **21**(2), 485–500 (2022).
[25]Y. Zhang, F. Avallone, and S. Watson, "Wind turbine blade trailing edge crack detection based on airfoil aerodynamic noise: An experimental study," Appl. Acoust. **191**, 108668 (2022).
[26]Y. Zhang, F. Avallone, and S. Watson, "An aeroacoustics-based approach for wind turbine blade damage detection," J. Phys.: Conf. Ser. **2265**(2), 022088 (2022).
[27]Y. Zhang, F. Avallone, and S. Watson, "Leading edge erosion detection for a wind turbine blade using far-field aerodynamic noise," Appl. Acoust. **207**, 109365 (2023).
[28]C. Lv, X. Ye, Y. Wu, W. Cheng, and C. Li, "Impact of trailing edge cracks on the aerodynamic performance and noise of offshore wind turbine airfoils," Phys. Fluids **37**(4), 047135 (2025).
[29]P. Lutzmann, B. Göhler, C. A. Hill, and F. van Putten, "Laser vibration sensing at Fraunhofer IOSB: Review and applications," Opt. Eng. **56**(3), 031215 (2016).
[30]B. Oswald-Tranta, "Temperature reconstruction of infrared images with motion deblurring," J. Sens. Sens. Syst. **7**(1), 13–20 (2018).
[31]N. Varghese, M. M. Mahesh, and A. N. Rajagopalan, "Fast motion-deblurring of IR images," IEEE Signal Process. Lett. **29**, 459–463 (2022).
[32]D. Kim, G. S. Lee, and C. Cheong, "Inflow broadband noise from an isolated symmetric airfoil interacting with incident turbulence," J. Fluids Struct. **55**, 428–450 (2015).
[33]T. F. Brooks and T. H. Hodgson, "Trailing edge noise prediction from measured surface pressures," J. Sound Vib. **78**(1), 69–117 (1981).
[34]S. M. Hasheminejad, T. P. Chong, G. Lacagnina, P. Joseph, J.-H. Kim, K.-S. Choi, M. Omidyeganeh, A. Pinelli, and O. Stalnov, "On the manipulation of flow and acoustic fields of a blunt trailing edge aerofoil by serrated leading edges," J. Acoust. Soc. Am. **147**(6), 3932–3947 (2020).
[35]S. Oerlemans, "Wind turbine noise: Primary noise sources," Report No. NLR-TP-2011-066 (National Aerospace Laboratory, 2011); available at http://hdl.handle.net/10921/117.
[36]T. F. Brooks, D. S. Pope, and M. A. Marcolini, *Airfoil Self-Noise and Prediction* (National Aeronautics and Space Administration, 1989).
[37]M. Kiya, H. Tamura, and M. Arie, "Vortex shedding from a circular cylinder in moderate-Reynolds-number shear flow," J. Fluid Mech. **101**, 721–735 (1980).
[38]B. A. Younis and V. P. Przulj, "Computation of turbulent vortex shedding," Comput. Mech. **37**(5), 408–425 (2006).
[39]P. E. Hancock and P. Bradshaw, "Turbulence structure of a boundary layer beneath a turbulent free stream," J. Fluid Mech. **205**, 45–76 (1987).
[40]M. Matsubara and P. H. Alfredsson, "Disturbance growth in boundary layers subjected to free-stream turbulence," J. Fluid Mech. **430**, 149–168 (2001).
[41]A. F. P. Ribeiro, F. L. dos Santos, K. Venner, and L. D. de Santana, "Numerical study of inflow turbulence distortion and noise for airfoils," Phys. Fluids **35**(11), 115112 (2023).
[42]L. Botero-Bolívar, F. L. Dos Santos, C. H. Venner, and L. de Santana, "Increase of unsteady pressure at a trailing edge due to inflow turbulence," AIAA J. **60**(12), 6798–6813 (2022).
[43]F. L. dos Santos, L. Botero-Bolívar, C. H. Venner, and L. D. de Santana, "Wall-pressure spectra, spanwise correlation, and far-field noise measurements of a NACA 0008 airfoil under uniform and turbulent inflows," Appl. Acoust. **211**, 109546 (2023).
[44]L. Botero-Bolívar, F. L. dos Santos, C. H. Venner, and L. D. de Santana, "Trailing-edge far-field noise and noise source characterization in high inflow turbulence conditions," J. Acoust. Soc. Am. **155**(2), 803–816 (2024).
[45]M. L. Beninati and J. S. Marshall, "An experimental study of the effect of free-stream turbulence on a trailing vortex," Exp. Fluids **38**(2), 244–257 (2005).
[46]L. Botero-Bolívar, F. L. Dos Santos, C. H. Venner, and L. de Santana, "Influence of the freestream turbulence on wall-pressure fluctuations along an airfoil chord," AIAA J. **61**(5), 2309–2313 (2023).
[47]C. Norberg, "Interaction between freestream turbulence and vortex shedding for a single tube in cross-flow," J. Wind Eng. Ind. Aerodyn. **23**, 501–514 (1986).
[48]I. Khabbouchi, H. Fellouah, M. Ferchichi, and M. S. Guellouz, "Effects of free-stream turbulence and Reynolds number on the separated shear layer from a circular cylinder," J. Wind Eng. Ind. Aerodyn. **135**, 46–56 (2014).
[49]G. Chen, X. Li, R. Xue, K. He, H. Wang, and X. Liang, "Effects of incoming free-stream turbulence on the flow dynamics of a square finite wall-mounted cylinder," Phys. Fluids **35**(2), 025140 (2023).
[50]K. Branner and A. Ghadirian, "Database about blade faults," DTU Wind Energy Report No. E-0067, December 2014.
[51]S. Oerlemans, "Detection of aeroacoustic sound sources on aircraft and wind turbines," Ph.D. thesis (University of Twente, 2009).
[52]P. Sijtsma, "Phased array beamforming applied to wind tunnel and fly-over tests," SAE Paper No. 2010-36-0514, 2010.
[53]G. Berkooz, P. Holmes, and J. L. Lumley, "The proper orthogonal decomposition in the analysis of turbulent flows," Annu. Rev. Fluid Mech. **25**(1), 539–575 (1993).
[54]B. W. Van Oudheusden, F. Scarano, N. P. Van Hinsberg, and D. W. Watt, "Phase-resolved characterization of vortex shedding in the near wake of a square-section cylinder at incidence," Exp. Fluids **39**(1), 86–98 (2005).
[55]R. Merino-Martínez, A. Rubio Carpio, L. T. Lima Pereira, S. van Herk, F. Avallone, D. Ragni, and M. Kotsonis, "Aeroacoustic design and characterization of the 3D-printed, open-jet, anechoic wind tunnel of Delft University of Technology," Appl. Acoust. **170**, 107504 (2020).
[56]R. Merino-Martínez, P. Sijtsma, A. R. Carpio, R. Zamponi, S. Luesutthiviboon, A. M. N. Malgoezar, M. Snellen, C. Schram, and D. G. Simons, "Integration methods for distributed sound sources," Int. J. Aeroacoust. **18**(4–5), 444–469 (2019).
[57]Q. Ye, F. F. J. Schrijer, and F. Scarano, "Boundary layer transition mechanisms behind a micro-ramp," J. Fluid Mech. **793**, 132–161 (2016).
[58]F. H. Clauser, "The turbulent boundary layer," Adv. Appl. Mech. **4**, 1–51 (1956).
[59]G. D. Huffman and P. Bradshaw, "A note on von Kármán's constant in low Reynolds number turbulent flows," J. Fluid Mech. **53**(1), 45–60 (1972).
[60]S. C. C. Bailey, M. Vallikivi, M. Hultmark, and A. J. Smits, "Estimating the value of von Kármán's constant in turbulent pipe flow," J. Fluid Mech. **749**, 79–98 (2014).
[61]R. Maddahian, A. Kebriaee, B. Farhanieh, and B. Firoozabadi, "Analytical investigation of boundary layer growth and swirl intensity decay rate in a pipe," Arch. Appl. Mech. **81**(4), 489–501 (2011).
[62]K. A. Thole and D. G. Bogard, "High freestream turbulence effects on turbulent boundary layers," J. Fluids Eng. Trans. ASME **118**(2), 276–284 (1996).
[63]B. Brzek, S. Torres-Nieves, J. Lebrn, R. Cal, C. Meneveau, and L. Castillo, "Effects of free-stream turbulence on rough surface turbulent boundary layers," J. Fluid Mech. **635**, 207–243 (2009).
[64]S. N. Sharp, S. Neuscamman, and Z. Warhaft, "Effects of large-scale free stream turbulence on a turbulent boundary layer," Phys. Fluids **21**(9), 095105 (2009).
[65]O. M. Fouatih, B. Imine, and M. Medale, "Numerical/experimental investigations on reducing drag penalty of passive vortex generators on a NACA 4415 airfoil," Wind Energy **22**(7), 1003–1017 (2019).
[66]T. Cebeci, *Analysis of Turbulent Flows with Computer Programs* (Butterworth-Heinemann, 2013).

[67]D. Yuan, J. Deng, R. Han, D. Li, and S. Tan, "Experimental study on flow structures of central blockage accidents in a rectangular channel using PIV and POD," Ann. Nucl. Energy **153**, 108037 (2021).
[68]Q. Zhang and Y. Liu, "Influence of incident vortex street on separated flow around a finite blunt plate: PIV measurement and POD analysis," J. Fluids Struct. **55**, 463–483 (2015).
[69]M. Stöhr, R. Sadanandan, and W. Meier, "Phase-resolved characterization of vortex-flame interaction in a turbulent swirl flame," Exp. Fluids **51**(4), 1153–1167 (2011).
[70]Y. Yang, S. Pröbsting, Y. Liu, H. Zhang, C. Li, and Y. Li, "Effect of dual vortex shedding on airfoil tonal noise generation," Phys. Fluids **33**(7), 075102 (2021).
[71]H. Cao, T. Zhou, Y. Zhang, and M. Zhang, "An experimental investigation of aerodynamic and aeroacoustic performance of a wind turbine airfoil with trailing edge serrations," J. Acoust. Soc. Am. **151**, 1211–1222 (2022).
[72]B. Turhan, Z. Wang, and I. Gursul, "Coherence of unsteady wake of periodically plunging airfoil," J. Fluid Mech. **938**, 1–32 (2022).
[73]B. Gibeau and S. Ghaemi, "The mode B structure of streamwise vortices in the wake of a two-dimensional blunt trailing edge," J. Fluid Mech. **884**, A12 (2020).
[74]G. Taherian, M. Nili-Ahmadabadi, M. H. Karimi, and M. R. Tavakoli, "Flow visualization over a thick blunt trailing-edge airfoil with base cavity at low Reynolds numbers using PIV technique," J. Visualization **20**(4), 695–710 (2017).
[75]M. Drela, "XFOIL: An analysis and design system for low Reynolds number airfoils," in *Low Reynolds Number Aerodynamics* (Springer, 1989), pp. 1–12.
[76]J. E. Ffowcs Williams and D. L. Hawkings, "Sound generation by turbulence and surfaces in arbitrary motion," Philos. Trans. R. Soc. London, Ser. A **264**(1151), 321–342 (1969).
[77]C. A. Echeverri-Londoño and A. E. González-Fernández, "Model for the prediction of noise from wind turbines," Rev. Fac. Ing. **2018**(88), 55–65.
[78]V. B. Nukala and S. P. Maddula, "Influence of rotor solidity on trailing edge noise from wind turbine blades," Adv. Aerodyn. **2**(1), 15 (2020).
[79]W. Z. Shen, N. Yunakov, J. F. Cao, and W. J. Zhu, "Development of a general sound source model for wind farm application," Renewable Energy **198**, 380–388 (2022).
[80]R. Krishnamurthy, A. Choukulkar, R. Calhoun, J. Fine, A. Oliver, and K. S. Barr, "Coherent Doppler lidar for wind farm characterization," Wind Energy **16**, 189–206 (2013).
[81]G. Cortina and M. Calaf, "Turbulence upstream of wind turbines: A large-eddy simulation approach to investigate the use of wind lidars," Renewable Energy **105**, 354–365 (2017).